A Thesis for the Degree of Doctor of Philosophy

Structure determination of the type III effector protein XopQ from *Xanthomonas oryzae* pv. *oryzae* and its functional implications

벼 흰잎마름병균 *Xanthomonas oryzae* pv. *oryzae* type III effector XopQ의 구조 및 기능 연구

2014 년 8 월

서울대학교 대학원

농생명공학부 응용생명화학전공

유 상 헌

ABSTRACT

Structure determination of the type III effector protein XopQ from *Xanthomonas oryzae* pv. *oryzae* and its functional implications

SANGHEON YU
Department of Agricultural Biotechnology
The Graduate School
Seoul National University

Many Gram-negative bacteria deliver their virulence factors into host cells through a secretion system. Those factors, called effector proteins, are involved in the pathogenicity in host cells by interfering with various cellular events. The phytopathogen *Xanthomonas oryzae* pv. *oryzae* uses a type III secretion system to inject its effectors, but the functional roles of these proteins remain largely uncharacterized. Type III effector protein $XopQ^{XOO}$ from *X. oryzae* pv. *oryzae* and XopQ homologs from other phytopathogens have been predicted to be nucleoside hydrolases (NH) based on their sequence similarities. The overall structure of $XopQ^{XOO}$ is homologous to that of NHs, including a metal-binding site, but differs in its

oligomeric state and active site topology. Further analysis indicated that antiparallel β-strands commonly found in NHs adjacent to the active site loop are replaced in $XopQ^{XOO}$ with a short loop, causing the active site loop to adopt a conformation distinct from that of NHs. Thus, the catalytic residues emanating from the respective active site loop of NHs are absent in the putative active site of $XopQ^{XOO}$. Consistent with these structural features, a functional assay indicated that $XopQ^{XOO}$ does not exhibit NH activity.

Based on the conservation of a Ca^{2+} coordination shell of a ribose-binding site and the spacious active site in $XopQ^{XOO}$, It could be hypothesized that a novel compound containing a ribosyl moiety could serve as a substrate for $XopQ^{XOO}$. The crystal structure of $XopQ^{XOO}$ in complex with adenosine diphosphate ribose (ADPR) was determined. ADPR, which is involved in regulating cytoplasmic Ca^{2+} concentrations in eukaryotic cells, is bound to the active site of $XopQ^{XOO}$ with its ribosyl end tethered to the Ca^{2+} coordination shell. The binding of ADPR is further stabilized by interactions mediated by hydrophobic residues that undergo ligand-induced conformational changes. These data, together with a functional analysis, showed that $XopQ^{XOO}$ is capable of binding a novel chemical bearing a ribosyl moiety, thereby providing the first step toward understanding the functional role of $XopQ^{XOO}$.

Key words: effector protein; pathogenicity; type III secretion system; *Xanthomonas* outer protein Q; nucleoside hydrolase; adenosine diphosphate ribose

Student Number: 2007-21398

CONTENTS

LIST OF FIGURES

LIST OF TABLES

LIST OF ABBREVIATIONS

MAMP	microbe-associated molecular pattern
PAMP	pathogen-associated molecular pattern
PRR	pattern-recognition receptor
PTI	PAMP-triggered immunity
R	resistance
Avr	avirulence
ETI	effector-triggered immunity
T3SS	type III secretion system
Xoo	*Xanthomonas oryzae* pv. *oryzae*
Xop	*Xanthomonas* outer protein
NH	nucleoside hydrolase
PCR	polymerase chain reaction
TEV	tobacco etch virus
DTT	dithiothreitol
PEG	polyethylene glycol
CU-NH	cytidine and uridine-specific nucleoside hydrolase
IAG-NH	inosine, adenosine, and guanosine-specific nucleoside hydrolase

IG-NH	inosine and guanosine-specific nucleoside hydrolase
IU-NH	inosine and uridine-specific nucleoside hydrolase
DNS	3,5-dinitrosalicylic acid
ADPR	adenosine diphosphate ribose
cADPR	cyclic adenosine diphosphate ribose
iPMP	N^6-isopentenyladenosine-5'-monophosphate
RMSD	root-mean-square deviation

INTRODUCTION

Plants are exposed to various microbial pathogens in nature. To protect themselves from plant pathogenic bacteria, plants possess effective defense systems (Chisholm at el, 2006). The primary immune response of plants is elicited by recognizing microbial common features such as lipopolysaccharides, peptidoglycans, lipoproteins, and flagella. These molecules are common in almost all bacteria for survival but not present in plants. Thus, plants can easily perceive plant pathogenic bacteria. These are called microbe-associated molecular pattern (MAMP) or pathogen-associated molecular pattern (PAMP) (Zhang and Zhou, 2010). MAMPs or PAMPs are recognized specifically by plant cell-surface receptors, so called pattern-recognition receptor (PRR). This recognition triggers plant immune responses referred to as PAMP-triggered immunity (PTI) (Zhang and Zhou, 2010). PTI is achieved through MAP kinase, transcriptional activation of immune-related genes, production of reactive oxygen species such as nitric oxide, and deposition of callose at sites of infection to reinforce the cell wall (Nurnberger et al., 2004).

To circumvent PTI, many plant pathogenic Gram-negative bacteria use complex secretion machines, allowing pathogen growth and replication

(Chrisholm et al, 2006; Pieterse et al, 2009). Three different types of secretion machines, type III, type IV, and type VI secretion systems, have been known (Christie et al., 2005; Filloux et al., 2008; Galán and Wolf-Watz, 2006). Bacterial pathogens deliver diverse their proteins into host plant cells using these secretion systems to modulate a variety of cellular functions. These proteins are called bacterial effectors and have a variety of functional roles in host cells. Effectors interfere with normal metabolisms in plant cells to result in pathogenic consequences (Grant et al., 2006; Mudgett, 2005).

Bacterial pathogens suppress primary defenses in plants. However, plants developed a more specialized mechanism, the adaptive immune response, to detect microbes. Plants contain resistance (R) proteins to recognize so called avirulence proteins (Avr) and subvert PTI. Therefore, activation of R protein-mediated immune response, referred to as effector-triggered immunity (ETI), suppresses microbial growth (Chrisholm et al, 2006).

The type III secretion system (T3SS) consists of a supramolecular structure resembling a bacterial flagellum. The T3SS is encoded by *hrp* (*h*ypersensitive *r*esponse and *p*athogenicity) genes (Gurlebeck et al., 2006). The T3SS is used to deliver diverse bacterial proteins into host plant cells to

subvert host defense responses (Galán and Wolf-Watz, 2006). The study of type III effector proteins has provided understanding of the function of the secretion system and also the aspects of the interaction between a host and a pathogen. However, it is difficult for many effectors to identify biochemical functions in proteins. Structural analyses of the effector proteins can sometimes provide clues about their biochemical and molecular functions. For example, a T3SS effector, *Pseudomonas syringae* AvrPtoB structurally mimics and functions as RING-domain type of E3 ubiquitin ligases in spite of no sequence similarities between them (Janjusevic et al., 2006). Since many effector proteins modulate complex cellular functions through coordinated activities, it is often confusing to know precise biochemical roles of effectors. Effectors have no biochemical functions in bacteria but functions in host cells. Therefore, it is difficult to determine biochemical functions of effectors through *in vitro* experiments.

Xanthomonas oryzae pv. *oryzae* (Xoo) is a causative agent of bacterial blight in rice (Adhikari et al., 1995; Niño-Liu et al., 2006). Bacterial blight is one of the most serious diseases in rice. Xoo is a good model organism to understand fundamental aspects of plant-bacteria interactions. The T3SS encoded in the *hrp* locus of Xoo plays an essential role in pathogenesis (Kamdar et al., 1993). However, the functional roles of

T3SS-dependent effector proteins remain largely uncharacterized. Previously, several effector proteins from *Xanthomonas* species, designated *Xanthomonas* outer proteins (Xop), were identified as T3SS substrates, and their functions were tentatively assigned by sequence similarity with functionally known proteins (Jiang et al., 2009; Furutani et al., 2009; Roden et al., 2004). In particular, $XopQ^{XOO}$ was identified as an effector protein from *X. oryzae* pv. *oryzae* KACC10331. It exhibits high sequence similarity to *X. campestris* pv. *vesicatoria* XopQ (94% sequence identity) and *Pseudomonas syringae* pv. *tomato* HopQ1-1 (61% sequence identity) (Jiang et al., 2009; Roden et al., 2004; Wei et al., 2007). Both XopQ and HopQ1-1 proteins are effectors that have been annotated as nucleoside hydrolases (NHs) based on their sequence similarities to known NHs (Jiang et al., 2009; Roden et al., 2004). NHs are present in a wide range of organisms including prokaryotes and higher eukaryotes, and catalyze the hydrolysis of the *N*-glycosidic bond in nucleosides. Although XopQ is predicted as NHs based on the primary amino acid sequence similarity, it shares approximately 20% of the sequence identity with other NHs, and the conserved DXDXXXDD motif of NHs, which is responsible for chelation of a Ca^{2+} ion, is somewhat different from that of $XopQ^{XOO}$.

Recently, it was reported that the effectors XopQ and HopQ1-1 are

phosphorylated at their own conserved serine residue in plant cells, which facilitates interacting with host 14-3-3 proteins (Giska et al., 2013; Li et al., 2013; Teper et al., 2014). This interaction suppresses the innate immune response or effector-triggered immunity of plants (Hann et al., 2013; Sinha et al., 2013). However, the molecular function of these effectors has yet to be resolved.

In this thesis, a crystal structure of $XopQ^{XOO}$ was determined at 1.6 Å resolution, and subsequently structural features of $XopQ^{XOO}$ complexed with the adenosine diphosphate ribose (ADPR) were characterized. $XopQ^{XOO}$ indeed shares a structural similarity with that of NHs and its Ca^{2+}-chelating residues are completely conserved with those of NHs in spite of the difference of the primary sequence. However, a functional analysis suggests that $XopQ^{XOO}$ is not a cognate NH although it shares structural similarity with NHs. The most notable structural feature of $XopQ^{XOO}$ is the size of the putative active site, which is approximately three-fold larger than that of typical NHs. Given the conservation of the Ca^{2+} coordination shell for ribose-binding and the spacious active site, a novel compound containing a ribosyl moiety could serve as a substrate for $XopQ^{XOO}$. This hypothesis is consistent to some extent with recent studies showing that HopQ1-1 is capable of hydrolyzing cytokinin precursors (Hann et al., 2013).

Substrates of $XopQ^{XOO}$ were screened by soaking crystals of $XopQ^{XOO}$ in solutions containing substrate candidates bearing a ribosyl moiety. It was characterized that the binding of ADPR in the Ca^{2+} coordination shell of $XopQ^{XOO}$, although cyclic adenosine diphosphate ribose (cADPR) was employed as the substrate. Interestingly, cADPR and ADPR are directly involved in regulating the Ca^{2+} concentration of the cytoplasm (Guse, 2005), which is one of the key events in the immune response elicited by pathogen invasion of a host plant (Cheval et al., 2013; DeFalco et al., 2010; Reddy et al., 2011). The complex form of $XopQ^{XOO}$ was compared with that of its native form, and a functional analysis was performed to determine the possible functional role of $XopQ^{XOO}$.

MATERIALS AND METHODS

1. Construction and purification of XopQ^{XOO}

XOO4466, a gene of XopQ^{XOO} (GenBank ID: YP_203105), was used as a template for polymerase chain reaction (PCR) with sequence-specific primers (Table 1). The resulting PCR product was then cloned into the pET28 vector (Novagen) for the N-terminal His-tag followed by a tobacco etch virus (TEV) protease cleavage site. These plasmids were transformed into *E. coli* BL21 (DE3) cells (Novagen) and used for protein production as described below. After failure to obtain a crystal of full-length XopQ(Full)^{XOO} (Met1 to Arg464), various constructs truncating either the N- or C-terminal region of XopQ^{XOO} were constructed. Among them, XopQ(D85)^{XOO} (Asp85 to Gly460) was successfully used for structure determination in this study.

The N-terminal His-tagged XopQ(D85)^{XOO} was expressed in methionine auxotroph *E. coli* B834 (DE3) cells (Novagen). Cells harboring the plasmid were grown at 37°C supplemented with 0.2 mM selenomethionine until the OD_{600} reached 0.6, and were then induced at 20°C for 14 h with the addition of 0.5 mM isopropyl-L-thio-β-D-galactopyranoside. To produce crystals for ligand soaking, the BL21 (DE3)

Table 1. List of *XOO4466* and *yeiK* primers used in this study

XOO4466^{FULL}	Forward	5′- GAATTCCATATGCAGCCCACCGC -3′
	Reverse	5′- AACCGCTCGAGGCGCGCATGTTCC -3′
XOO4466^{D85}	Forward	5′- CTGGCCGAGCTCGGCCATATGGACACGCCCGTGCTG -3′
(for D85)	Reverse	5′- CAGCACGGGCGTGTCCATATGGCCGAGCTCGGCCAG -3′
XOO4466^{D85}	Forward	5′- AGCAGGACGAGGGGTAACATGCGCGC -3′
(for G460)	Reverse	5′- GCGCGCATGTTACCCCTCGTCCTGCT -3′
YeiK	Forward	5'- GAATTCCATATGGAAAAGAGAAAAATTATTC -3'
	Reverse	5'- AACCGCTCGAGTTAATGGGTTTTGATG -3'

cells harboring the plasmid was grown and induced in Luria-Bertani (LB) medium. Cells were harvested, resuspended, and sonicated in buffer A [50 mM Tris (pH 8.0) and 2 mM dithiothreitol (DTT)]. The N-terminal His-tagged protein was purified using an immobilized metal affinity column (GE Healthcare) with buffer B (buffer A containing additional 0.5 M immidazole) followed by gel filtration chromatography on a Superdex 200 column (GE Healthcare) with buffer C [20 mM Tris (pH 8.0) and 2 mM DTT]. The N-terminal His-tag was removed at this stage by mixing the purified protein (0.3 mg/mL) with the TEV protease (1:40 w:w) overnight at 22°C. The His-tag-free XopQ(D85)^{XOO} was further purified using immobilized metal affinity chromatography and concentrated to 5 mg/mL for crystallization.

2. Crystallization and structure determination

Selenomethionine-labeled and native XopQ(D85)^{XOO} was crystallized using the sitting drop vapor diffusion method by mixing equal volumes of protein solution and crystallization solution containing 8.5% (w/v) polyethylene glycol (PEG) 1000, 8.5% (w/v) PEG 8000, 15% (v/v) glycerol, and 10 mM $CaCl_2$ (Fig. 1). For structural determination, multi-wavelength diffraction data to 1.6 Å resolution were collected at 100 K on beamline BL-1A at the Photon Factory (Tsukuba, Japan) without the

Fig. 1. Crystals of Selenomethionine-labeled XopQ(D85)^{XOO}.

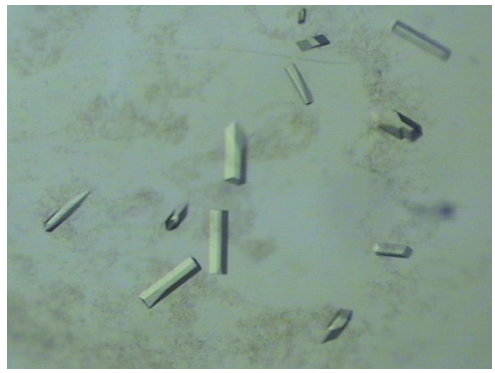

Fig. 2. Diffraction of Selenomethionine-labeled XopQ(D85)^{XOO}.

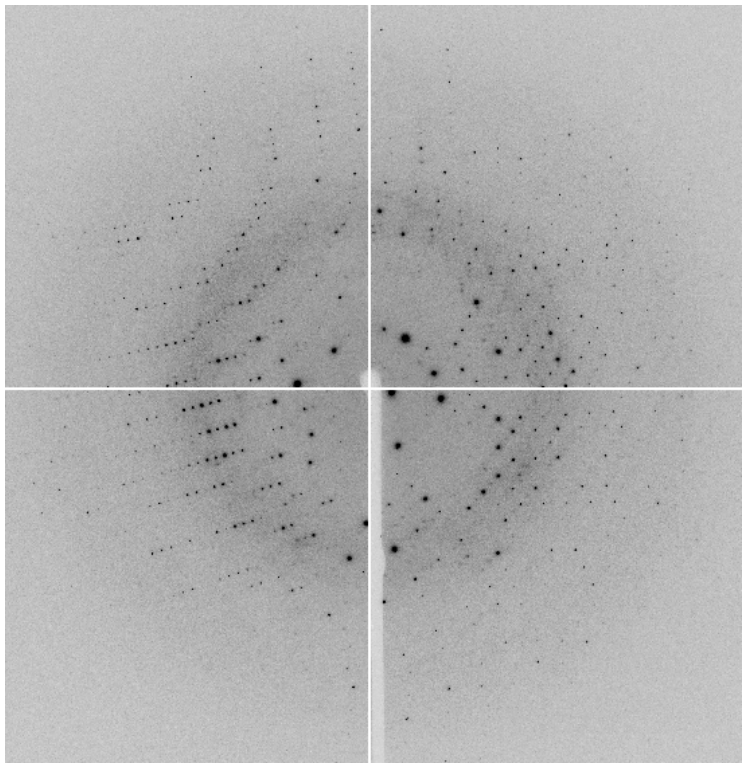

addition of cryoprotectant (Fig. 2). To find out a substrate, several chemicals were used for soaking experiments. XopQ(D85)^{XOO} crystals were soaked for 1~5 min in the crystallization solution additionally containing 5 mM uridine monophosphate, 5 mM uridine triphosphate, 5 mM *S*-adenosyl methionine, or 5 mM nicotinamide mononucleotide. The crystals were also soaked for 1 min or 30 min in the mother liquor containing 50 mM or 5 mM nicotinamide adenine dinucleotide, respectively and for 1 min or 10 min in the mother liquor containing 20 mM or 5 mM nicotinamide adenine dinucleotide phosphate, respectively. After failure to see the electron density fitted to any chemical above, native crystals were soaked for ~5 min in the mother liquor containing an additional 4 mM cADPR (Sigma-Aldrich) and 20% glycerol for cryoprotection to obtain the structure of XopQ(D85)^{XOO}-cADPR complex. Single-wavelength data to a resolution of 2.1 Å were collected at 100K on beamline 7A at the Pohang Accelerator Laboratory, Korea. The data collected were indexed, integrated, and scaled with HKL2000 (Table 2; Otwinowski and Minor, 1997). The space group of the XopQ(D85)^{XOO} crystal and the XopQ(D85)^{XOO}-cADPR complex was $P2_1$ and $P2_12_12_1$, respectively; an asymmetric unit consists of one monomer and two monomers due to different space groups and cell dimensions.

The XopQ(D85)^{XOO} structure containing eight methionine residues

Table 2. Crystallographic data and refinement statistics

	Apo-XopQ(D85)^{XOO}			XopQ(D85)^{XOO}-ADPR complex
	Peak	**Inflection**	**Remote**	
Data collection				
Wavelength (Å)	0.9789	0.9791	0.9639	0.9793
Space group	$P2_1$			$P2_12_12_1$
Cell dimensions	47.8, 70.5, 49.1, β=99.9°			48.0, 73.8, 201.9, $\alpha=\beta=\gamma$=90°
Resolution (Å)	50.0-1.60 (1.66-1.60) [a]	50.0-1.70 (1.76-1.70)[a]	50.0-1.80 (1.86-1.80)[a]	50.0-2.1 (2.18-2.10) [a]
R_{merge} [b]	0.082 (0.717)	0.083 (0.560)	0.076 (0.436)	0.153 (0.856)
$I/\sigma I$	26.3 (2.4)	25.3 (3.1)	28.5 (4.3)	18.9 (3.25)
Completeness (%)	99.8 (99.6)	99.9 (99.7)	99.9 (99.9)	99.8 (100.0)
Redundancy	7.5 (7.5)	7.6 (7.5)	7.6 (7.6)	12.7 (12.9)
Refinement				
Resolution (Å)	50.0-1.6			36.3-2.1
No. unique reflections	42,434			42,892
R_{work} [c]/R_{free} [d] (%)	0.202/0.235			20.16/25.31
No. atoms				
Protein	2,688			5,365
Ca	1			3
Ligand				36
Water	176			188
B-factors				
Protein	21.9			19.7
Ca	10.5			24.2
Ligand				25.4
Water	26.8			20.6
RMSD				
Bond lengths (Å)	0.018			0.007
Bond angles (deg)	1.743			1.116
Ramanchandran analysis				
Favored (%)	97.1			97.4
Allowed (%)	2.6			2.3
Outlier (%)	0.3[e]			0.3[e]
PDB ID	4KL0			4P5F

[a] Values in parenthesis are for a highest-resolution shell.

[b] $R_{merge}=\sum_{hkl}\sum_i|I_i-\langle I\rangle|\sum_{hkl}\sum_i I_i$.

[c] $R_{work}=\sum_{hkl}||F_{obs}|-k|F_{calc}||/\sum_{hkl}|F_{obs}|$.

[d] R_{free} was calculated using 10% of data excluded from refinement.

[e] Leu148 associated with a clear density is in an outlier region.

was solved by the multiwavelength anomalous dispersion method (Hendrickson et al., 1985) using SOLVE (Terwilliger and Berendzen, 1999) and RESOLVE (Terwilliger, 2000) for phasing and density modification, respectively. Then, the structure of the XopQ(D85)^{XOO}-ADPR complex was determined by molecular replacement using PHENIX (Adams et al., 2004) with the apo-structure of XopQ(D85)^{XOO} as a search model. The models were refined using PHENIX and manually rebuilt with COOT (Emsley and Cowtan, 2004). Crystallographic data and refinement statistics are listed in Table 2. The stereochemistry of the refined model was checked using MolProbity (Chen et al., 2010), which indicated that Leu148 is well stabilized with a clear density but is in an outlier region. Figures were prepared using PyMOL (DeLano WL, The PyMOL Molecular Graphics System), ChemDraw (Li et al., 2004), Chimera (Pettersen et al., 2004), and TopDraw of the CCP4 suite (Collaborative Computational Project No. 4, 1994). Structure analysis was carried out using the CCP4 suite.

3. Nucleoside hydrolase activity

Previous bioinformatic analysis classified XopQ^{XOO} as a NH member (Roden et al., 2004) based on its sequence homology within a Thr111–Asp399 region with known NH enzymes (Fig. 3). To validate this

proposal, I carried out an assay for NH activity using XopQ^{XOO}. As a control, activities of the cytidine- and uridine-specific (CU)-NH YeiK (Giabbai and Degano, 2004a) were also measured.

The *yeiK* gene from *E. coli* BL21 (DE3) was amplified by PCR with sequence-specific primers (Table 1) and subcloned into the pET28 vector as described above. For the NH activity assay, the C-terminal His-tagged XopQ(Full)^{XOO} and N-terminal His-tagged YeiK protein were expressed in *E. coli* BL21 (DE3) cells in LB medium and purified using the HisTrap HP column and Superdex 200 column with 50 mM HEPES, pH 7.3. In particular, YeiK was purified in a modified protocol from procedures previously described (Giabbai and Degano, 2004b). The assay was carried out at 30°C in 1 mL of the reaction mixture containing 50 mM HEPES (pH 7.3), 3 μM XopQ(Full)^{XOO} or YeiK, and 5 mM of the indicated substrate. After 1 h, the reaction mixture was treated with 4 mL of 3,5-dinitrosalicylic acid (DNS) reagent [0.7% (w/v) DNS, 20.4% (w/v) sodium potassium tartrate, 0.5% (w/v) sodium metabisulfite, 1.3% (w/v) sodium hydroxide, and 0.5% (v/v) phenol]. The reaction was terminated by boiling the mixture for 10 min, and the resulting 3-amino-5-nitrosalicylic acid produced by reacting DNS with a reducing ribose was measured at 540 nm (Miller, 1959).

4. cADPR hydrolysis assay

The observation that the active site of XopQ(D85)^{XOO} contains ADPR but not cADPR led us to hypothesize that XopQ(D85)^{XOO} catalyzes the hydrolysis of cADPR. To test this hypothesis, I measured the cADPR hydrolytic activity of XopQ^{XOO} as well as that of its homolog HopQ1-1.

For the assay, C-terminal His-tagged, full-length XopQ(Full)^{XOO} and N-terminal His-tagged XopQ(D85)^{XOO}, as well as C-terminal His-tagged HopQ1-1, were expressed in BL21(DE3) in LB medium and purified using a HisTrap HP column and a Superdex 200 column. The HopQ1-1 gene from *P. syringae* pv. *tomato* DC3000 was amplified by PCR and subcloned into the pET41 vector. Typically, the assay was performed at 25°C for 20 min in 0.2 mL of a reaction mixture containing 20 mM Tris (pH 8.0), 2 mM DTT, 1.0 or 3.5 μM protein, 0.1 mM $CaCl_2$, and 50 μM cADPR or 50 μM cytokinin precursor, N^6-isopentenyladenosine-5'-monophosphate (iPMP; OlChemIm Ltd). The reaction product was then analyzed by HPLC using an Inno C18 column (5 μm; 250 × 4.6 mm) (Innopia) at a flow rate of 0.7 mL/min for cADPR and ADPR and of 1.0 mL/min for iPMP. cADPR and ADPR were separated using a gradient of buffer D [20 mM KH_2PO_4 (pH 6.0)] and buffer E [20 mM KH_2PO_4 (pH 6.0) and 10% MeOH]. iPMP elution was performed using a gradient of 1% acetic acid and 100% MeOH.

All chemicals were detected by measuring the absorbance of the eluate at 254 nm.

To test possibility that another divalent cation rather than a Ca^{2+} ion is needed to be the activity of XopQ, 20 mL of the purified protein solution was dialyzed in 1 L of 50 mM Tris (pH 7.5), 0.2 M NaCl, and 10 mM EDTA at 4°C overnight and subsequently in 1 L of 50 mM Tris (pH 7.5), and 0.2 M NaCl in twice. The naked protein solution was further dialyzed in 0.5 L of 20 mM Tris (pH 7.5), 0.1 M NaCl, 1.0 mM DTT, and 1.0 mM $MgCl_2$, $MnCl_2$, or $SrCl_2$, and 20 mM Bis-tris (pH 6.5), 0.1 M NaCl, and 1.0 mM $(NH_4)_2Fe(SO_4)_2$ at 4°C overnight. The enzymatic reaction was carried out at 25°C for 20 min in 0.2 mL of a reaction mixture additionally containing 50 μM cADPR. For other cations, the assay could not be performed because $XopQ(FULL)^{XOO}$ protein was precipitated during dialysis in 0.5 L of 20 mM HEPES (pH 7.5) , 0.1 M NaCl, and 1.0 mM $ZnCl_2$ or $CoCl_2$, and 20 mM Bis-tris (pH 6.5), 0.1 M NaCl, and 1.0 mM $CuCl_2$.

Fig. 3. Multiple sequence alignment of $XopQ^{XOO}$ with various NHs. Sequences of NHs are IAG-NH (UniProt ID: Q9GPQ4), IG-NH (Q57X73), IU-NH (Q27546), and CU-NH (P33022). Highly conserved residues are shown in red and boxed in blue, and strictly conserved residues are shown on a red background. Secondary structural elements and residue number for $XopQ^{XOO}$ (PDB ID 4KL0) are given for the corresponding $XopQ^{XOO}$ sequences, with indications of disordered regions in green bars. Different notions are indicated by magenta asterisks and circles for the Ca^{2+}- and ribose-interacting residues in $XopQ^{XOO}$, respectively, and those in cyan for the respective residues in NHs. Residues overlaid with yellow at both the N- and C-termini represent regions not used for the $XopQ(D85)^{XOO}$ structure. This figure was prepared using ESPript (Gouet et al., 1999).

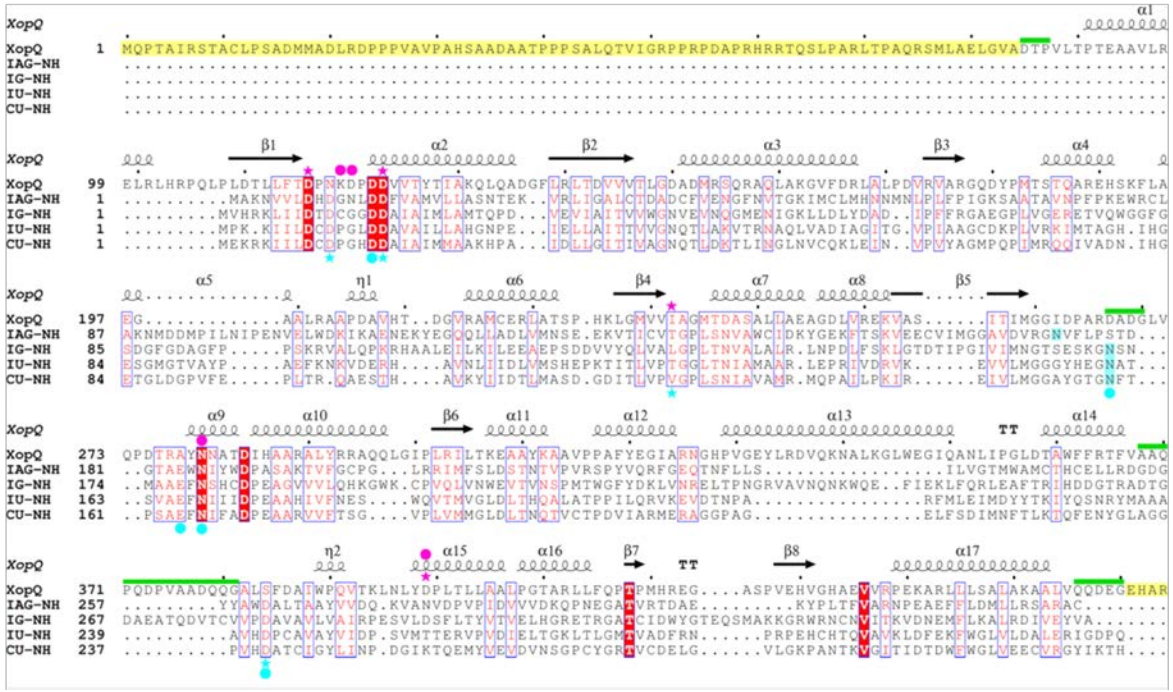
XopQ
IAG-NH
IG-NH
IU-NH
CU-NH

RESULTS AND DISCUSSION

1. Overall structure and calcium-binding site of XopQ^{XOO}

XopQ(85)^{XOO} is folded into a single domain (Fig. 4A) composed of 17 α-helices and eight β-strands (Fig. 3). The core structure is the α–β–α sandwich fold, in which eight β-strands form a central parallel β-sheet, except for an antiparallel β7. The central β-sheet is flanked by helices aligned along the β-strands: α2, α3, and α15 on one side and α6–α10 on the opposite side of the β-sheet facing the protein surface. Other α-helices (α12–α14) are juxtaposed to α2, α3, and α15 in an α–β–α sandwich fold and apparently form an additional layer of a segment and protrude from the core domain (Fig. 4B).

A cleft exists in the middle of the α–β–α core domain to which a metal ion is bound (Fig. 4B). In particular, the metal-binding site is located at the region surrounded by the C-terminal ends of β1 and β4, and the N-terminal ends of α2 and α15 (Fig. 5). The presence of a metal ion was first indicated by the coordination geometry and its distance to the nearby residues and water molecules, with a strong density in a *Fo–Fc* map (Fig. 5). Subsequently, inductively coupled plasma atomic emission spectroscopy analysis showed that a Ca^{2+} ion is present in an equimolar ratio with purified

Fig. 4. Crystal structure of XopQ(85)^{XOO}. (A) Overall structure of XopQ(85)^{XOO} is shown in a different orientation, with the central β-strands in red. (B) A surface representation of XopQ(85)^{XOO} and IAG-NH (PDB ID: 1HP0; Versées et al., 2001) is displayed with indication of the active site. A cleft represents the active site, and a substrate analog, a 3'-deaza-adenosine, is shown at the IAG-NH cleft.

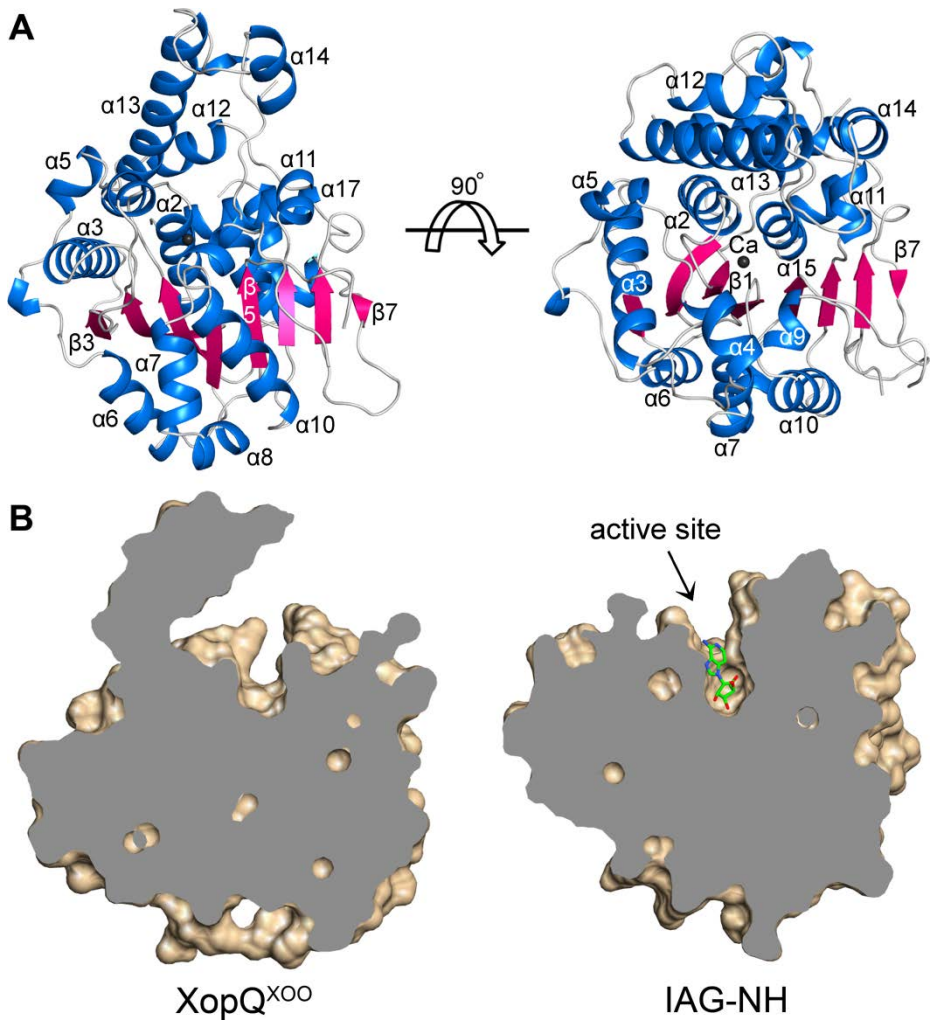
A
α14
α13
α12
α5
α11
α17
α2
α3
β5
β7
β3
α7
α6
α10
α8
90°
α12
α14
α5
α13
α11
α2
Ca
β7
α3
β1
α15
α4
α9
α6
α10
α7
B
active site
XopQXOO
IAG-NH

Fig. 5. Metal-binding site of XopQ(85)^{XOO}. (A) The metal-binding site in XopQ(85)^{XOO} is displayed in a stereo view, with interatomic distances shown (Å). Different color codes used are a gray circle for the Ca^{2+} ion-bound, a green circle for two water molecules, and a red circle for a putative catalytic water molecule, as suggested in IAG-NH. Note that positions for water molecules in green correspond to the two hydroxyl groups of ribose in the IAG-NH structure. (B) The Ca^{2+} ion (gray circle) and three water molecules (red circles) are overlaid with the *Fo–Fc* electron density map contoured at 4.0 σ.

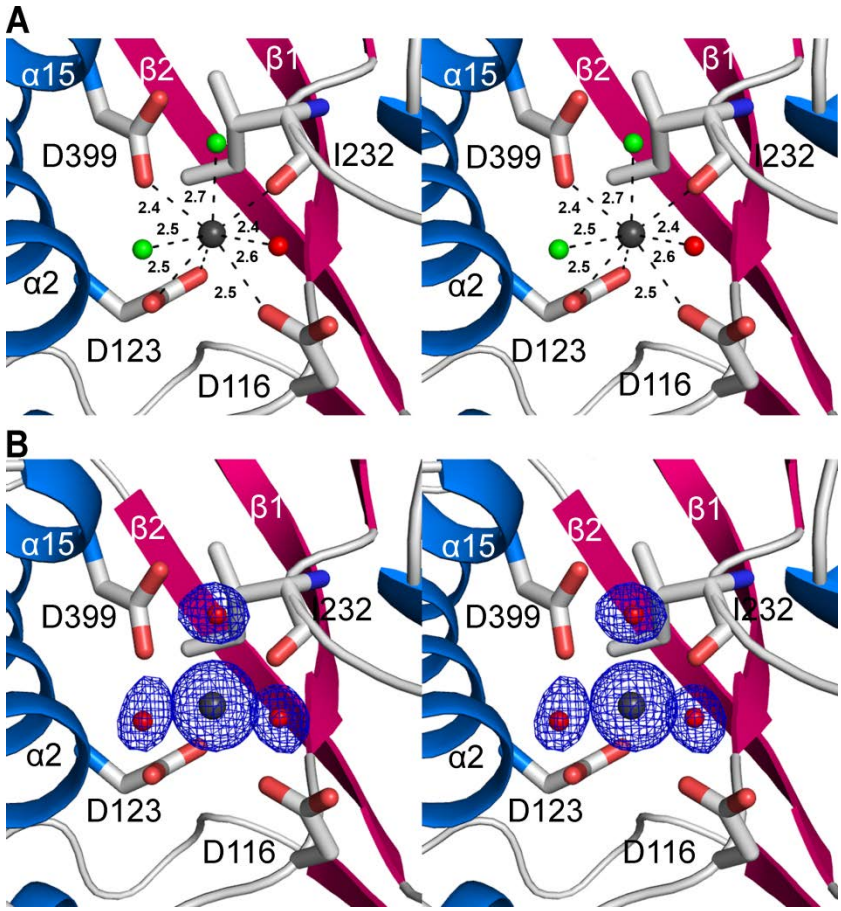
A
α15
β2
β1
D399
I232
2.4
2.7
2.5
2.4
2.5
2.6
2.5
α2
D123
D116
B
α15
β2
β1
D399
I232
α2
D123
D116

Table 3. Quantities of elements in the solution containing 0.17 mM XopQ

Elements	Mean (ppb)	Elements	Mean (ppm)
Mg	< 5	Al	< 0.5
Ti	< 5	Ca	7.759
Mn	< 5	Na	46.62
Co	< 5	Si	< 0.5
Ni	21.32		
Cu	632.3		
Zn	129.1		
As	< 5		
Se	< 5		
Rb	< 5		
Mo	< 5		
Pd	< 5		
Ag	< 5		
Cd	< 5		
Os	17.75		
Au	< 5		
Pb	10.84		

Left and right columns are analyzed by an inductively coupled plasma (ICP) mass spectroscopy and ICP atomic emission spectroscopy, respectively.

XopQ(85)^{XOO}, and also that a Ca^{2+} ion did not originate from the crystallization solution containing 10 mM $CaCl_2$ but rather from the cell growth media (Table 3). Therefore, I concluded that a Ca^{2+} ion occupies the metal-binding site in XopQ(85)^{XOO}. The Ca^{2+}-coordination shell consists of three aspartate residues, a carbonyl oxygen of the main chain, and three water molecules. The Ca^{2+} ion interacts within 2.5 Å with the carboxylate of Asp116 in a loop between β1 and α2, Asp123 on α2, and Asp399 on α15. The main chain carbonyl oxygen of Ile232, as well as three water molecules, is also within a distance of 2.7 Å from the Ca^{2+} ion.

2. Oligomeric state of XopQ(85)^{XOO} and NHs

The structure of XopQ(85)^{XOO} is homologous with that of NH enzymes, consistent with sequence similarity. A root-mean-square deviation between XopQ(85)^{XOO} and various types of NHs are 2.4 Å for inosine, adenosine, and guanosine (IAG)-NH (PDB ID: 1HOZ; 240 C_α atoms; Versées et al., 2001), 2.2 Å for inosine and guanosine (IG)-NH (3FZ0; 248 C_α atoms; Vandemeulebroucke et al., 2010), 2.3 Å for inosine and uridine (IU)-NH (2MAS; 246 C_α atoms; Degano et al., 1998), and 2.5 Å for CU-NH (1Q8F; 242 C_α atoms; Giabbai and Degano, 2004a).

These structural similarities reside all over the α–β–α sandwich core

domain (Fig. 4B), except for two regions. First, α13 in XopQ(85)^{XOO} is approximately 10 residues longer than the corresponding helix in NHs. Structural elements involving α14 and a subsequent η2 are also unique only to XopQ(85)^{XOO} and are located on the outer surface of α13, causing this region to protrude from the rest of the protein (Fig. 4). Second, the most distinct difference between XopQ(85)^{XOO} and NHs is the presence of two antiparallel β-strands in NHs that precede a C-terminal β8 strand (Fig. 6). These antiparallel β-strands play a role in the formation of NH oligomeric conformations, in particular a tetrameric IG-NH, IU-NH, and CU-NH. Specifically, in the tetrameric conformation of NHs, a loop-2 following the second strand of the antiparallel β-strands makes intimate hydrophobic interactions with another loop, termed loop-3, from neighboring subunits (Fig. 6; Giabbai and Degano, 2004a; Shi et al., 1999; Vandemeulebroucke et al., 2010). In XopQ(85)^{XOO}, the two NH-unique antiparallel β-strands are replaced with an eight residue loop between β7 and β8, abolishing not only possible intersubunit interactions, but also causing a conformational difference in loop-3 (Gly260 to Asn280) between β5 and α9 relative to those in NHs (see below). In addition, noticeable changes were observed in the interaction environments of the surface in XopQ(85)^{XOO}. In other oligomeric NHs, intersubunit interactions are largely mediated by three

Fig. 6. Topology in XopQ(85)^{XOO} and IAG-NH. Topologies of XopQ^{XOO} and IAG-NH are shown, with α-helices and β-strands as blue cylinders and red arrows, respectively. The C-terminal antiparallel β-strands present in IAG-NH are indicated in green and the active site loop-3 is shown in magenta.

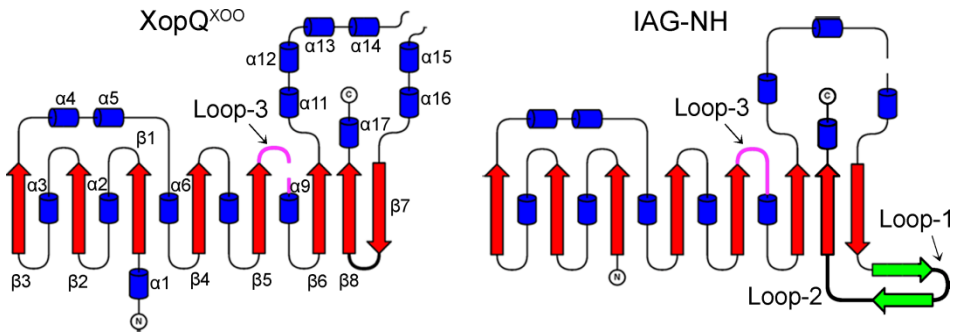
XopQ^XOO
α12
α13
α14
α15
α16
α4
α5
Loop-3
α11
α17
β1
α3
α2
α6
α9
β7
β3
β2
α1
β4
β5
β6
β8
N
C
IAG-NH
Loop-3
Loop-1
Loop-2
N
C

regions corresponding to a loop between β3 and α3, α-helix H1 between β4 and β5, and α-helix H2 between β5 and β6 (Fig. 6). In short, the six-residue-long loop protruding from one subunit makes extensive hydrophobic interactions with H2 in the adjacent subunit, and interactions between H1s in the neighboring subunits are also responsible for dimerization. In contrast, the respective loop of $XopQ^{XOO}$ does not extrude, and the chemical identity for residues in H1 and H2 are different from those of the NHs (Fig. 3). These structural alterations associated with sequence variations likely result in $XopQ(85)^{XOO}$ in a monomeric form.

3. Structural and functional features of native $XopQ^{XOO}$

The overall structure of $XopQ(85)^{XOO}$ resembles that of NHs, although a monomeric form of $XopQ^{XOO}$ is unique among other structurally homologous NHs. Therefore, I carried out a NH activity assay using $XopQ(FULL)^{XOO}$. Unexpectedly, $XopQ(FULL)^{XOO}$ failed to exhibit any NH activity using various nucleosides and their possible derivatives (Fig. 7). To identify any possible structural explanation for the absence of the expected NH activity in $XopQ^{XOO}$, the $XopQ(85)^{XOO}$ active site was compared with those of NHs (Fig. 8). In short, active site residues in NHs can be classified into three subgroups: Ca^{2+}-coordinating, ribose-binding, and base-

Fig. 7. Measurement of NH activity of $XopQ^{XOO}$ and YeiK using nucleosides and their derivatives. In a Control-A reaction, 5 mM D-ribose or uridine was present in the absence of $XopQ^{XOO}$ or YeiK, respectively, while substrate was absent in the reaction mixture for Control-B. A 3-amino-5-nitrosalicylic acid (ANS) produced by the copresence of DNS and a reducing ribose was measured at 540 nm, and its concentration was calculated by a standard curve using ribose. Unlike $XopQ^{XOO}$, YeiK exhibited its activity using cytidine and uridine.

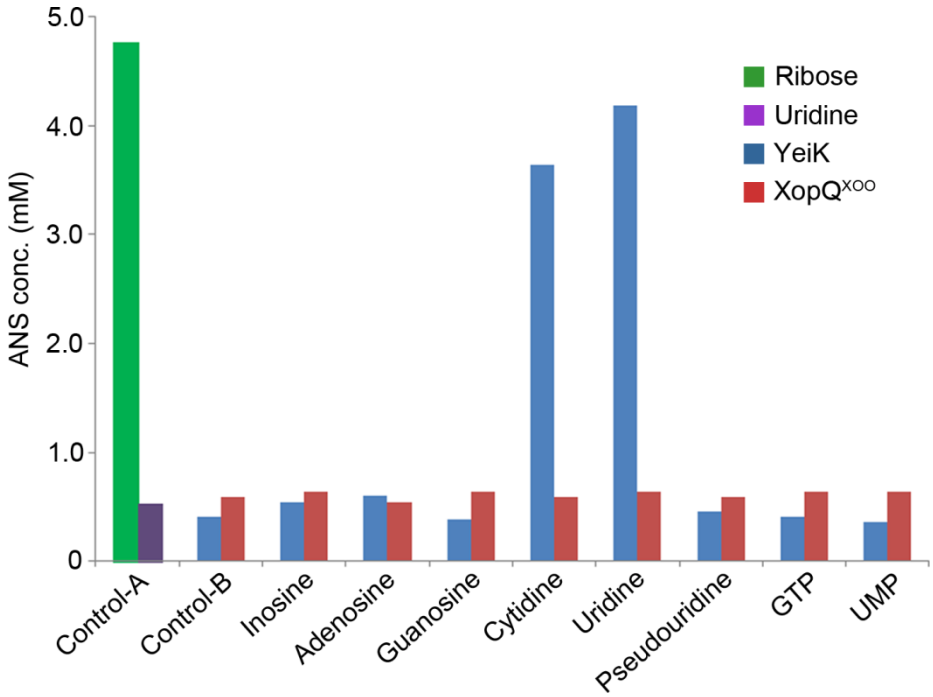
5.0
4.0
3.0
2.0
1.0
0
ANS conc. (mM)
Ribose
Uridine
YeiK
XopQXOO
Control-A
Control-B
Inosine
Adenosine
Guanosine
Cytidine
Uridine
Pseudouridine
GTP
UMP

interacting residues. Among them, the Ca^{2+}-coordinating and ribose-binding residues are well conserved in the structure and sequence of NHs (Figs. 3 and 8), consistent with the finding that NHs utilize a Ca^{2+} ion to interact with a ribosyl moiety. However, residues responsible for the binding of a nucleobase exhibit structural and sequence diversity among NHs (Figs. 3 and 8). For a better comparison, the active site of the IAG-NH enzyme is shown in Figure 9A (Versées et al., 2001). Specifically, two aspartate residues (Asp10 and Asp15 in IAG-NH, in a DXDXXXDD motif, a hallmark sequence of NHs), as well as a conserved aspartate (Asp261 in IAG-NH) and the carbonyl oxygen atom of the main chain (Thr137 in IAG-NH), coordinate with the Ca^{2+} ion in all NHs (Figs. 3, 8, and 9A). In addition, a proposed catalytic water molecule tethered to the metal-coordinating Asp10 in IAG-NH is also located in the coordination shell of various NHs (Figs. 8A and 9A) (Versées et al., 2001). Residues for the ribose-interacting subgroup are also well conserved in the structure and sequence among diverse NHs (Figs. 3 and 8). These residues form a hydrogen bond with the hydroxyl groups of a ribosyl moiety. In particular, the 5'-hydroxyl group of ribose was determined to be a key structural element for NHs to recognize nucleosides. Substrate affinity and product turnover numbers become significantly reduced by more than a hundredfold

Fig. 8. The active site of $XopQ^{XOO}$ and diverse NHs. (A) A substrate or its analog is shown in salmon. The Ca^{2+}-coordinating, ribose-binding, and nucleobase-stacking residues are shown in gray, green, and cyan, respectively. Water molecules are represented as red circles. (B) Residues involved in the active site are classified and listed.

A

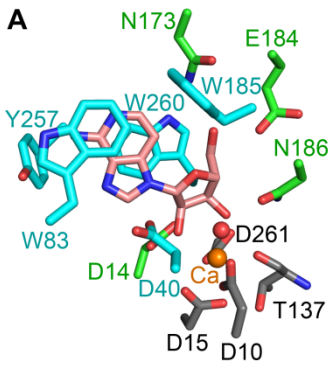

IAG-NH (PDB ID: 1HP0)

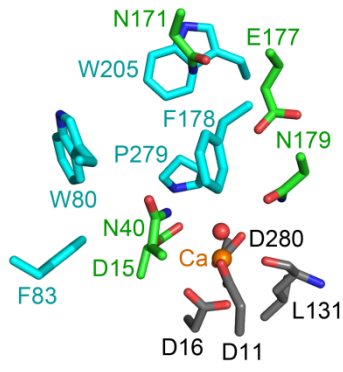

IG-NH (PDB ID: 3FZ0)

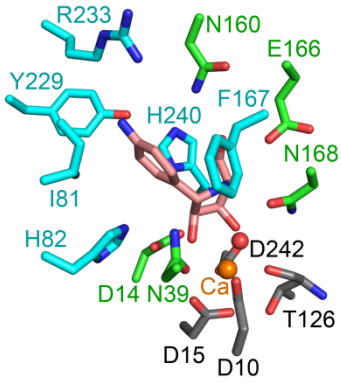

IU-NH (PDB ID: 2MAS)

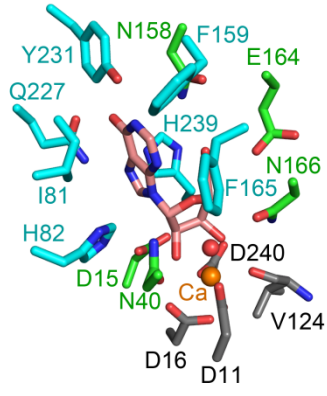

CU-NH (PDB ID: 3B9X)

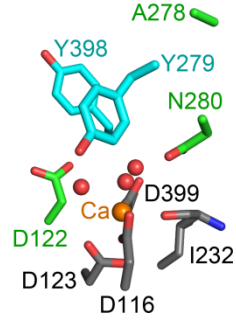

XopQ^{XOO}

B

	Ca^{2+}-chelating residues	Ribose-interacting residues	Nucleobase-interacting residues
IAG-NH	D10, D15, D261, T137	D14, N173, E184, N186	W83, W185, Y257, W260, D40
IG-NH	D11, D16, D280, L131	D15, N171, E177, N179, N40	W80, W205, F83, P279, F178
IU-NH	D10, D15, D242, T126	D14, N160, E166, N168, N39	I81, H82, F167, Y229, R233, H240
CU-NH	D11, D16, D240, V124	D15, N158, E164, N166, N40	I81, H82, F165, Q227, Y231, H239, F159
XopQ^{XOO}	D116, D123, D399, I232	D122, A278, N280	Y279, Y398

Fig. 9. Active sites in XopQ(85)^{XOO} and IAG-NH. (A) The active site of IAG-NH in complex with 3'-deaza-adenosine (PDB ID: 1HP0; Versées et al., 2001) is shown in a stereo view. The active site residues are indicated in different color codes: dark gray for the Ca^{2+}-chelating residues, green for the ribose-binding residues, and cyan for the nucleobase-interacting residues. A catalytic water molecule tethered by Asp10 is represented as a red circle. Loop-3 is highlighted in magenta. (B) Stereo view of the putative XopQ(85)^{XOO} active site is displayed. The color codes are identical with those in (A). To show the orientation of loop-3, zoom-out views are presented in Figure 8.

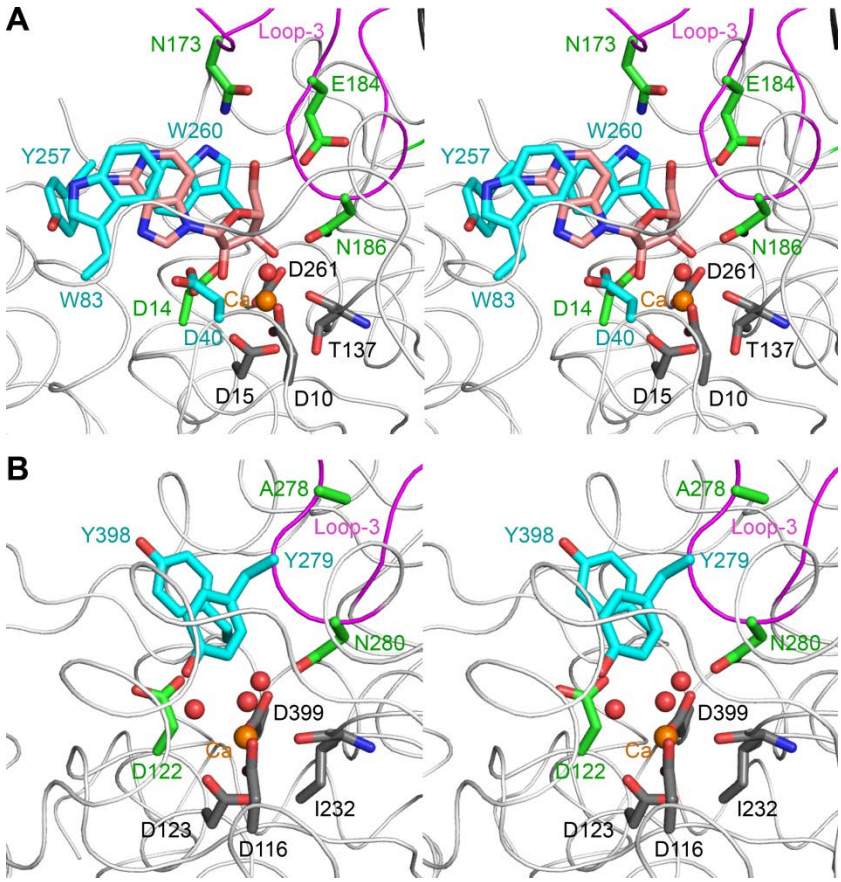
A
N173
Loop-3
E184
W260
Y257
N186
D261
W83
D14
Ca
D40
T137
D15
D10
B
A278
Y398
Loop-3
Y279
N280
D399
Ca
D122
I232
D123
D116

in IAG-NH and IG-NH relative to 5'-adenosine when 5'-deoxyadenosine is used as a substrate (Vandemeulebroucke et al., 2010; Versées et al., 2002). In IAG-NH, nucleoside binding is further facilitated by aromatic residues. Trp83 and Trp260 are in a position for the stacking interaction with a purine base of an adenosine analog, whereas Tyr257 is in a perpendicular position to the base (Fig. 9A). As a result, these aromatic residues enclose a base and form a cavity suitable for nucleobase binding. However, different binding modes of a ligand were characterized in IU-NH and CU-NH (Fig. 8).

In $XopQ^{XOO}$, the location of the Ca^{2+}-binding site is identical to that of NHs (Figs. 8A and 9). However, residues interacting with a bound metal are somewhat different from those of NHs identified in a pairwise sequence alignment (Fig. 3), but are equivalent in structure. Unlike NHs, the first and fourth aspartates in the DXXXDXDD motif of $XopQ^{XOO}$ (Asp116 and Asp123) are in the metal-coordination shell. Furthermore, Asp399 in $XopQ^{XOO}$ is involved in the Ca^{2+}-coordination shell, although this aspartate is not a residue conserved in NHs (Figs. 3 and 9B). Even with these variations, the geometry of the Ca^{2+}-coordination in $XopQ^{XOO}$ is almost superimposable to that of various NHs (Fig. 8A), as further exemplified in IAG-NHs (Fig. 9A). Specifically, Asp116, Asp123, Ile232, and Asp399 in $XopQ^{XOO}$ are structurally equivalent to Asp10, Asp15, Thr137, and Asp261,

respectively, in IAG-NH. Two water molecules in the metal-chelating shell of XopQ^{XOO} also correspond to the 2'- and 3'-hydroxyl groups of a ribose identified in IAG-NHs (Fig. 9). Moreover, the putative catalytic water molecule associated with Asp10 in IAG-NHs is also observed in XopQ^{XOO}, which is now held by Asp116.

Except for the metal-ligating residues, the putative active site in XopQ(85)^{XOO} exhibits noticeable alterations relative to that of NHs, mainly due to variations in sequence as well as conformation of loop-3. In NHs, two antiparallel β-strands adjacent to loop-3 restrict the conformational freedom of loop-3 and cause the residues in loop-3 to point into the active site, as observed in both the apo form and the complex with a substrate (Figs. 8A and 10A). However, absence of those structural elements in XopQ^{XOO} left the space vacant and allowed its loop-3 to occupy the space (Fig. 10B). As a result, the loop-3 in XopQ(85)^{XOO} adopts a conformation that is completely distinct from that in NHs, causing the active site to be in a widely open conformation, although the loop length is identical to that in NHs. Due to these conformational variations, active site residues from loop-3 identified in NHs cannot be found in XopQ(85)^{XOO}, but structural superposition suggests possible active site residues. For example, Asp122 and Asn280 in XopQ^{XOO} are only the residues structurally and in sequence

Fig. 10. Active site environments in IAG-NH and XopQ(85)^{XOO}. This presentation is a zoom-out view of Figure 7. (A) The active site of IAG-NH in complex with 3'-deaza-adenosine is shown in stereo view (PDB ID: 1HP0; Versées et al., 2001). Active site residues are indicated in different colors: dark gray for the Ca^{2+}-chelating residues, green for the ribose-binding residues, and cyan for the nucleobase-interacting residues. A catalytic water molecule tethered by Asp10 is represented as a red circle. Loop-3 is highlighted in magenta, and the NH-unique antiparallel β-strands are shown in green. (B) Stereo view of the putative XopQ(85)^{XOO} active site is displayed. The color codes are the same as those in (A). A short loop replacing the antiparallel β-strands of IAG-NH is shown in black.

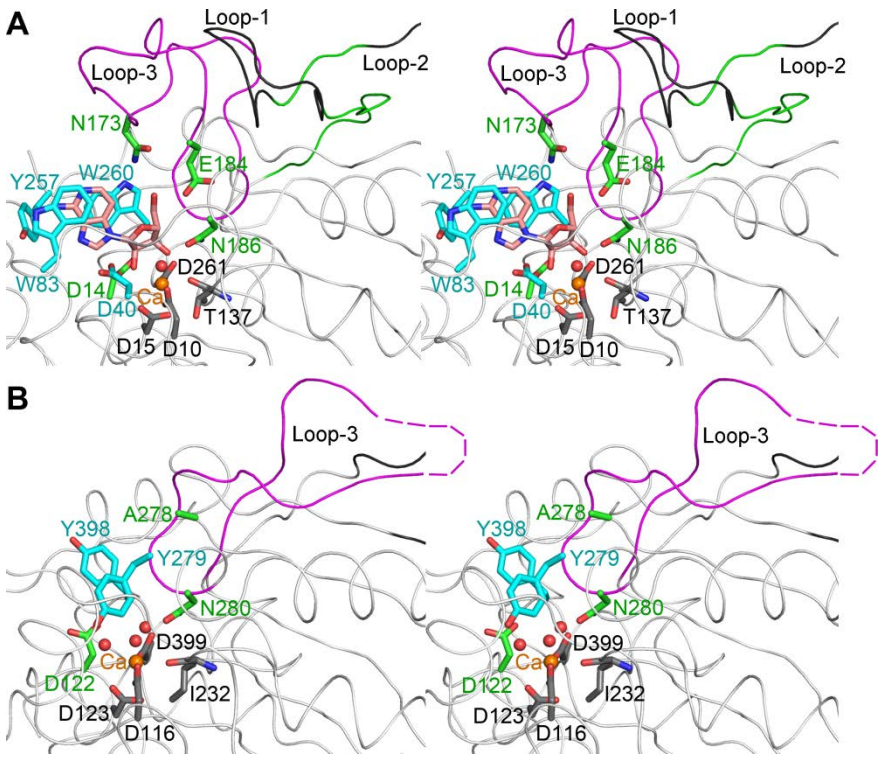
A
Loop-1
Loop-2
Loop-3
N173
E184
Y257
W260
N186
D261
W83
D14
Ca
D40
T137
D15
D10
B
Loop-3
A278
Y398
Y279
N280
D399
Ca
D122
I232
D123
D116

equivalent to aspartate and asparagine, respectively, that are conserved in NHs for the ribose-interacting residues (Fig. 9). Other ribose-interacting residues corresponding to Asn173 and Glu184 in loop-3 of IAG-NHs are no longer present in the vicinity of the $XopQ^{XOO}$ active site. Specifically, no structurally equivalent residue in $XopQ^{XOO}$ exists for Asn173 in IAG-NHs, and Ala278 in $XopQ^{XOO}$ corresponds to Glu184 in IAG-NHs. Given the proposed key role of these residues in recognizing the 5'-hydroxyl group of a ribose in a nucleoside (Vandemeulebroucke et al., 2010; Versées et al., 2002), a lack of these residues and a sequence change in $XopQ^{XOO}$ suggests that $XopQ^{XOO}$ likely has a low affinity for nucleosides or utilizes other molecules as substrates. Our analysis indicates that the active site environment of $XopQ^{XOO}$ is distinct from that in NHs, except for the metal-coordinating residues. Consistent with our functional analysis, a recent investigation from two independent research groups also noted that HopQ1-1, an $XopQ^{XOO}$ homolog, does not exhibit NH activity (Giska et al., 2013; Li et al., 2013). It is, however, not exclusive that no activity is because these proteins were expressed in and purified from *E. coli* cells, given that XopQ and HopQ1-1 in susceptible plant cells are phosphorylated at a conserved serine residue, which is critical to their own virulence (Giska et al., 2013; Li et al., 2013; Teper et al., 2014).

4. ADPR-binding and conformational changes in the XopQ(D85)^{XOO}–ADPR complex

In its native form, *i.e.*, its open conformation of another structural data set (Table 2; PDB ID 4P5F), XopQ(D85)^{XOO} is folded into an α–β–α sandwich domain with a protruding α-helical segment (α12–η4; Figs. 11A and 12). Here α12 of the data set 4P5F is equal to α13 of the data set 4KL0. A putative active site that binds a Ca^{2+} ion is located in the cleft between the α–β–α sandwich fold and the protruding α-helical segment. In the XopQ(D85)^{XOO}–ADPR complex, most of these secondary structural elements are conserved, but several regions are highly disordered (Fig. 12). Upon the binding of ADPR (see below), the protruding α-helical segment undergoes significant positional changes (Fig. 11B). Specifically, a long helix α12 in the protruding α-helical segment is kinked by approximately 37º at the middle of the helix (Lys339), and its C-terminal half, accompanied by α13 and η4, is shifted toward the Ca^{2+} binding site. These changes result in an ~11-Å movement of the loop between α12 and α13 onto the central β-sheet (Fig. 11B) and effectively seal off the active site cleft (Fig. 11C) to produce a close conformation. These conformational changes are not global and are localized to the vicinity of the active site. Therefore, structural superpositioning of the open and close forms revealed an RMSD

Fig. 11. Structural changes in the XopQ(D85)^{XOO}–ADPR complex. (A) Two different conformations of XopQ(D85)^{XOO}, as characterized in an asymmetric unit, are shown and labeled as the open and close forms. Ca^{2+} ion bound to the active site is presented as an orange circle, and ADPR is indicated in the close form. (B) Superposition of the two conformations is shown. Open and close forms are indicated in pink and cyan, respectively. (C) A surface representation of the two conformations is displayed. The active site of XopQ(D85)^{XOO} containing ADPR is in the close form.

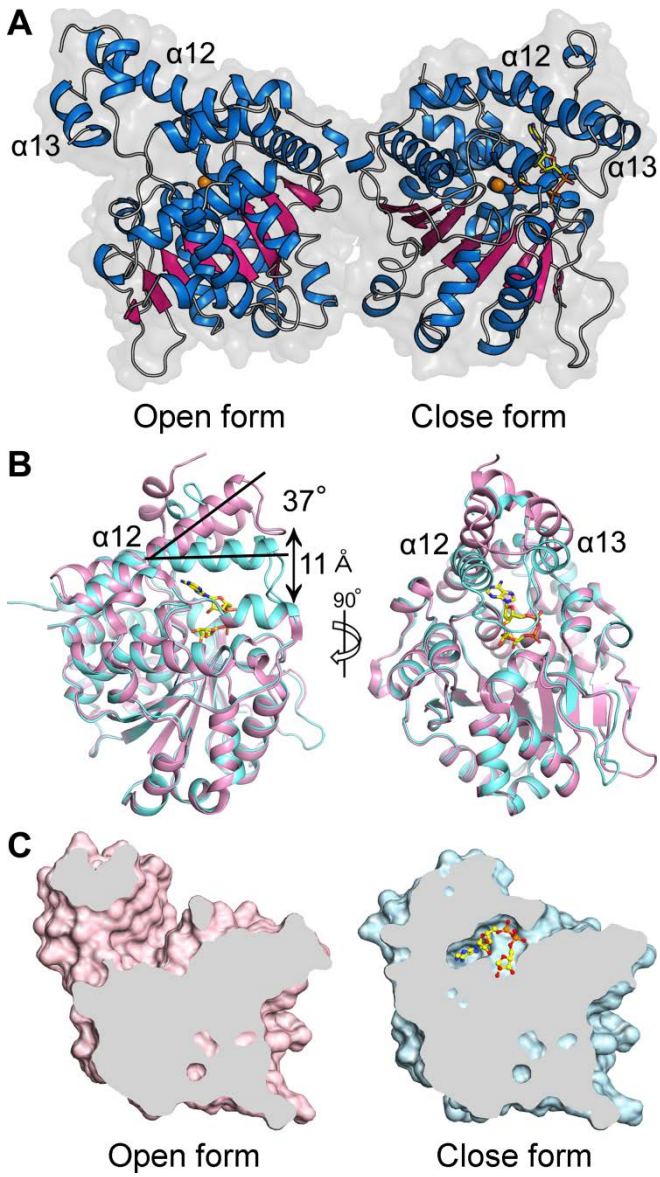
A
α12
α13
α12
α13
Open form
Close form
B
37°
α12
11 Å
90°
α12
α13
C
Open form
Close form

Fig. 12. Multiple sequence alignment of $XopQ^{XOO}$ with various homologous proteins. Sequences are as follows: XOO4466 (GenBank ID: YP_203105) for $XopQ^{XOO}$, HopQ1-1 (GenBank ID: NP_790716) from *P. syringae* pv. *tomato* DC3000, XC_3177 (YP_244241) for XopQ from *X. campestris* pv. *campestris* 8004, XCV4438 (YP_366169) for XopQ from *X. campestris* pv. *vesicatoria* 85-10, XAC4333 (NP_644627) for XopQ homolog from *X. axonopodis* pv. *citri* 306, and RSc0245 (NP_518366) for XopQ homolog from *Ralstonia solanacearum* GMI1000. Highly conserved residues are shown in red and boxed in blue, and strictly conserved residues are shown on a red background. Secondary structural elements and residue numbers for the close form of $XopQ(D85)^{XOO}$ are shown for the corresponding XOO4466 sequences, with disordered regions indicated by cyan bars. Magenta asterisks indicate Ca^{2+} chelating residues, and green triangles and blue circles represent residues mediating hydrogen bonds and hydrophobic interactions with ADPR, respectively. Residues overlaid with yellow at both the N- and C-termini represent regions not used in the $XopQ(D85)^{XOO}$ structure.

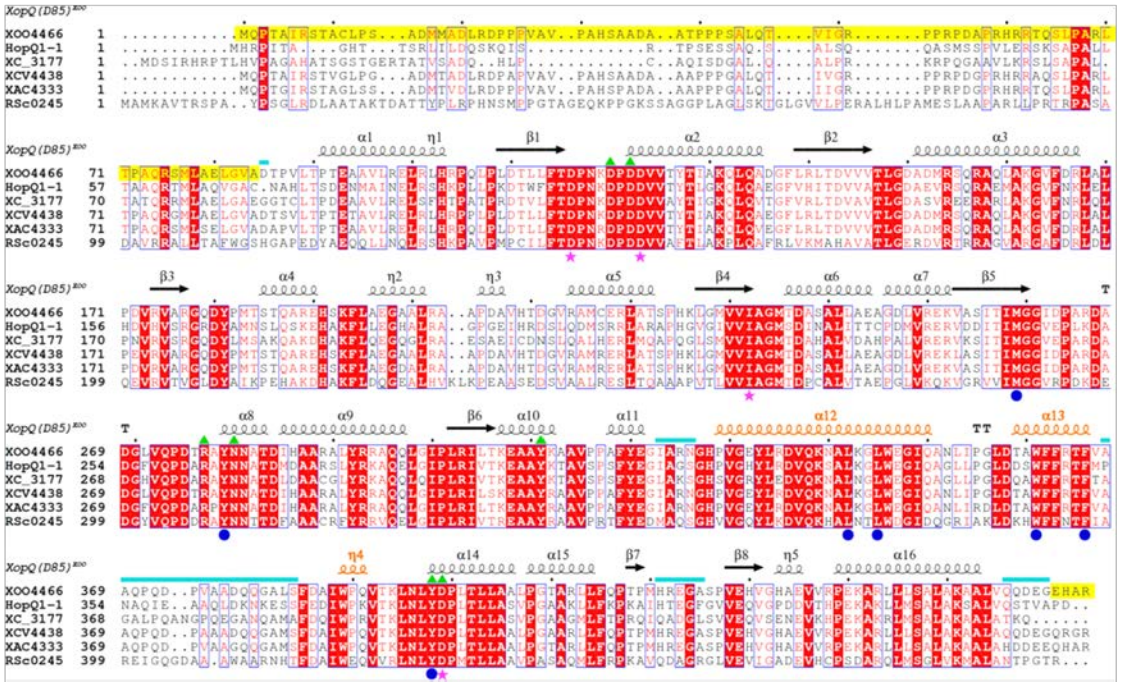
XopQ (D85)
XO04466
HopQ1-1
XC_3177
XCV4438
XAC4333
RSc0245

of 0.54 Å for 290 C_α atoms, excluding the α12 to η4 region.

An electron density corresponding to ADPR (Fig. 13A) was identified in the Ca^{2+} binding site, even though the XopQ(D85)^{XOO} crystal was soaked in 4 mM cADPR. HPLC analyses further indicated that the conversion of cADPR to ADPR cannot occur spontaneously in the soaking solution. Therefore, the observed electron density for ADPR suggests the possibility that crystalline XopQ(D85)^{XOO} exhibits hydrolytic activity for cADPR. Specifically, XopQ(D85)^{XOO} could cleave the glycosidic bond between the N^1 of the adenine moiety and the 5'-hydroxyl of the ribose$^{\beta}$ (the ribose moiety attached to the β-phosphate of the adenosine diphosphate of cADPR) of cADPR. ADPR binds to the active site in a bent configuration, in which the ribose$^{\beta}$ and adenosyl moieties at the other end are embedded in the innermost region of the Ca^{2+} binding site, and the diphosphate group that connects the two moieties is located in an outer region of the Ca^{2+} binding site. The 2'- and 3'-hydroxyl groups of ribose$^{\beta}$ are directly involved in coordinating Ca^{2+} ions (Fig. 13B and C). In addition to these interactions, the Ca^{2+} ion also coordinates within 2.6 Å with the carboxylate groups of Asp116, Asp123, Asp399, and the main chain carbonyl oxygen atom of Ile232 (Fig. 13C). This Ca^{2+} coordination shell in the XopQ^{XOO}–ADPR complex is essentially identical to that of the native form, except for the

Fig. 13. An ADPR-binding site in XopQ(D85)^{XOO}. (A) The Ca^{2+} ion (gray circle) and ADPR (yellow) are overlaid with the *Fo–Fc* electron density map contoured at 2.5 σ. The zoomed-in view in the right panel is shown with the Ca^{2+} coordinating residues. The ribose$^{\beta}$ moiety is indicated by an arrow. (B) The active sites of the open (pink) and close (green) forms are superimposed and shown in a stereo view. (C) A schematic diagram shows the interactions between XopQ(D85)^{XOO} and ADPR, with an indication of interatomic distance (Å). Different color codes are used in this scheme: Ca^{2+}-coordinating residues are shown in magenta, residues for hydrogen bonds are shown in green, and those for van der Waals interactions within 5.0 Å of ADPR are shown in blue. Water molecules are shown as red circles.

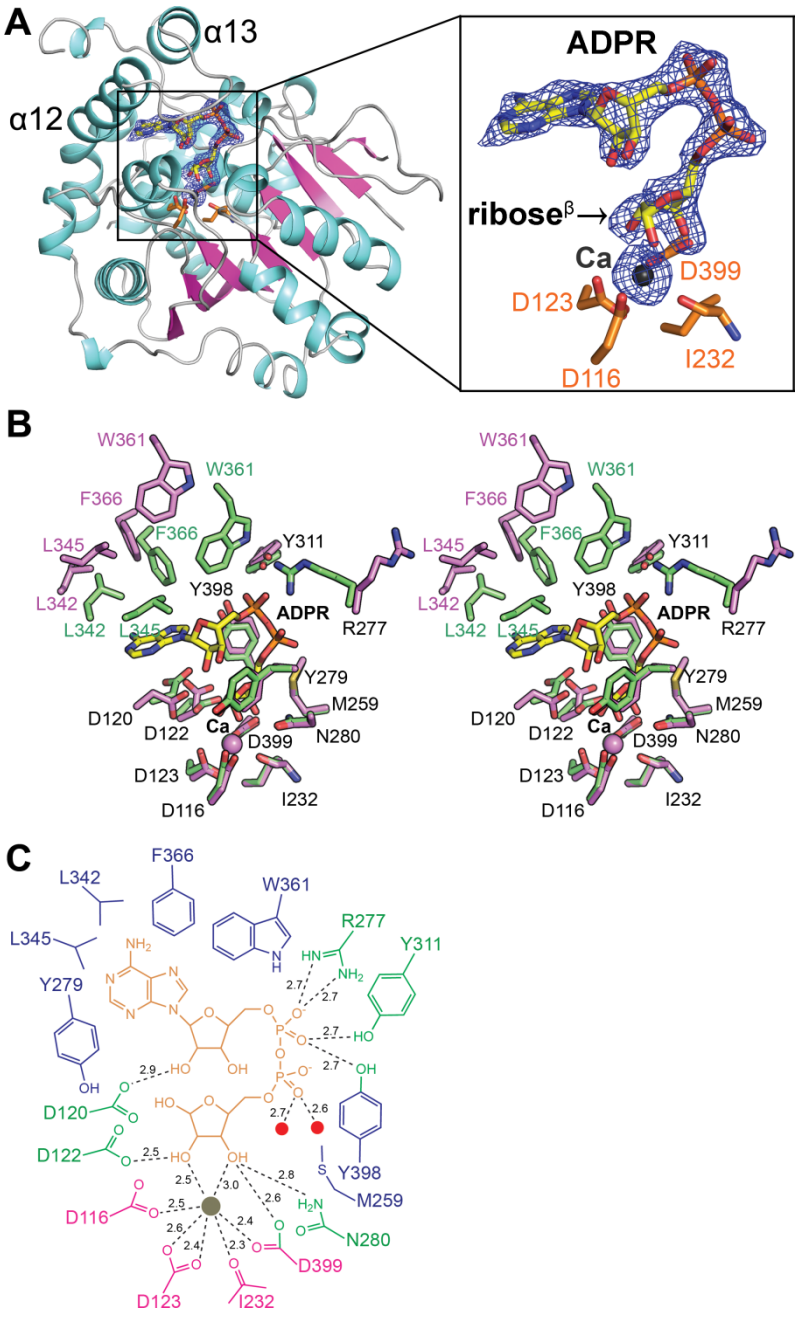
A
α13
α12
ADPR
ribose$^{\beta}$→
Ca
D399
D123
I232
D116
B
W361
W361
F366
F366
L345
Y311
Y398
L342
L342
L345
ADPR
R277
Y279
M259
D120
D122
Ca
D399
N280
D123
D116
I232
C
L342
F366
W361
L345
R277
Y311
Y279
D120
D122
Y398
M259
D116
N280
D399
D123
I232

interactions mediated by ribose$^{\beta}$.

The binding of ADPR is further stabilized by several nearby residues that are also conserved in other homologous proteins (Figs. 12 and 13C). Interestingly, residues in the vicinity of ribose$^{\beta}$ are located in nearly identical positions in both the native XopQ(D85)^{XOO} and the XopQ(D85)^{XOO}–ADPR complexes. In contrast, residues interacting with the adenosyl moiety emanate from the mobile α-helical segments and undergo large positional changes in a ligand-dependent manner (Fig. 13B). Specifically, ribose$^{\beta}$ interacts hydrophobically with Met259 and Tyr398, and its 2'- and 3'-hydroxyl groups are within hydrogen-bonding distance of Asp122 and Asn280, respectively. The adenosyl moiety of ADPR is within a hydrophobic patch consisting of Tyr279 on α8, Leu342 and Leu345 on α12, and Trp361 and Phe366 on α13. Of these five residues, all but Tyr279 move to the immediate vicinity of the adenosyl moiety through conformational changes. The 2'-hydroxyl group of ribose in the adenosyl moiety interacts with Asp120, the side chain of which adopts a different orientation relative to that in the native form. The diphosphate forms potential hydrogen bonds with the side chains of Tyr311, Tyr398, Arg277, and two water molecules. In particular, the side chain of Arg277 undergoes significant conformational change in the XopQ^{XOO}–ADPR complex.

5. cADPR-hydrolysis assay of XopQ^{XOO}

It was previously suggested that despite similarities in overall structure and Ca^{2+} binding geometry, the structural features and active site topology of XopQ(D85)^{XOO} are distinct from those of structurally homologous NHs. In particular, XopQ(D85)^{XOO} boasts a more spacious pocket adjacent to the bound Ca^{2+} ion (Fig. 14). In fact, consistent with these features, XopQ(FULL)^{XOO} and XopQ(D85)^{XOO}, as well as its ortholog HopQ1-1, do not exhibit NH activity (Fig. 7; Giska et al., 2013; Li et al., 2013). This indicates that XopQ^{XOO} may catalyze an as of yet uncharacterized reaction. Given that XopQ(D85)^{XOO} binds ADPR, which is a hydrolytic product of cADPR, it is plausible to think that XopQ^{XOO} and HopQ1-1 hydrolyze cADPR. HPLC analyses, however, indicated neither XopQ^{XOO} nor HopQ1-1 exhibit cADPR-hydrolysis activity under various conditions (Figs. 15 and 16). Moreover, contrary to previous observations for HopQ1-1 (Hann et al., 2013), no hydrolytic activity of XopQ^{XOO} toward the cytokinin precursor was observed under the current experimental conditions (Fig. 15B).

Given these data, I then hypothesized that XopQ^{XOO} is not an enzyme but rather an ADPR-binding protein. To test this hypothesis, ADPR was prepared by boiling 50 μM cADPR (Fig. 15A). The ADPR was

Fig. 14. A surface representation of NH and XopQ(D85)^{XOO}. NH (yellow; PDB ID 1HOZ; Versées et al., 2001) and XopQ(D85)^{XOO} (pink; PDB ID 4KL0; Yu et al., 2013) are shown after superimposition. A 3'-deaza-adenosine bound to NH is shown in green.

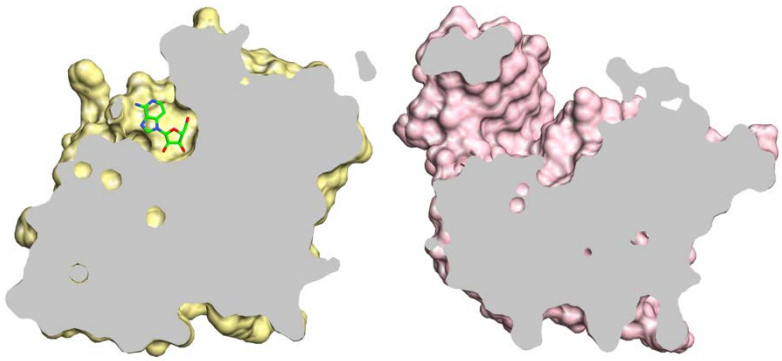
nucleoside hydrolase
XopQ^XOO

Fig. 15. HPLC analyses of the reaction products of $XopQ^{XOO}$ and HopQ1-1. (A) HPLC chromatograms are given for cADPR, ADPR, and the reaction products of $XopQ^{XOO}$ or HopQ1-1. ADPR was obtained by boiling 50 μM cADPR as described previously (Pawlikowska et al., 1996). For the enzyme reaction, cADPR was incubated with 1 μM $XopQ(FULL)^{XOO}$ or HopQ1-1 at 25ºC. (B) A solution of 3.5 μM $XopQ(FULL)^{XOO}$ and $XopQ(D85)^{XOO}$ was used in this reaction. Solutions containing 50 μM cADPR or 50 μM iPMP incubated with 3.5 μM $XopQ(FULL)^{XOO}$ or $XopQ(D85)^{XOO}$ were separated and analyzed by HPLC.

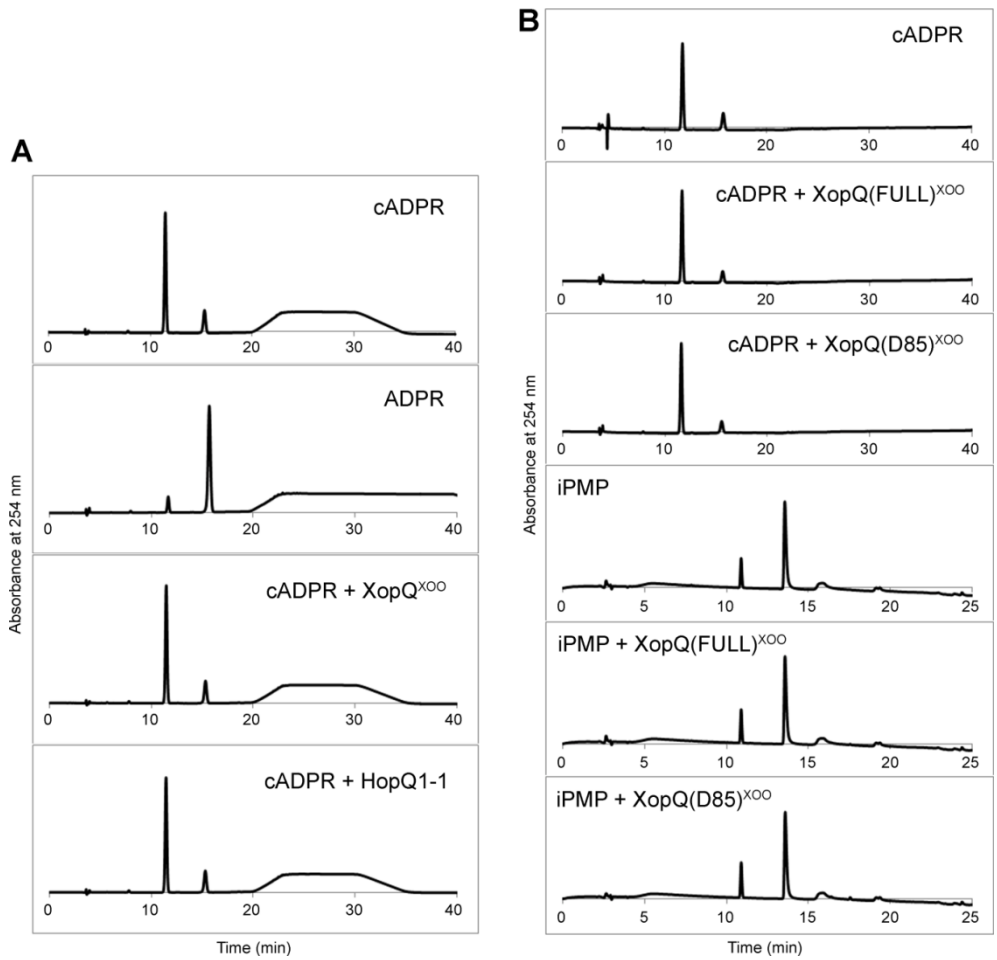
A
cADPR
ADPR
cADPR + XopQXOO
cADPR + HopQ1-1
Absorbance at 254 nm
Time (min)
B
cADPR
cADPR + XopQ(FULL)XOO
cADPR + XopQ(D85)XOO
iPMP
iPMP + XopQ(FULL)XOO
iPMP + XopQ(D85)XOO
Absorbance at 254 nm
Time (min)

Fig. 16. HPLC analyses of the reaction products of $XopQ^{XOO}$. HPLC chromatograms are given for cADPR and the reaction products of $XopQ(FULL)^{XOO}$. For the enzyme reaction, 50 μM cADPR was incubated with 9 μM $XopQ(FULL)^{XOO}$ at 25ºC, and separated and analyzed by HPLC.

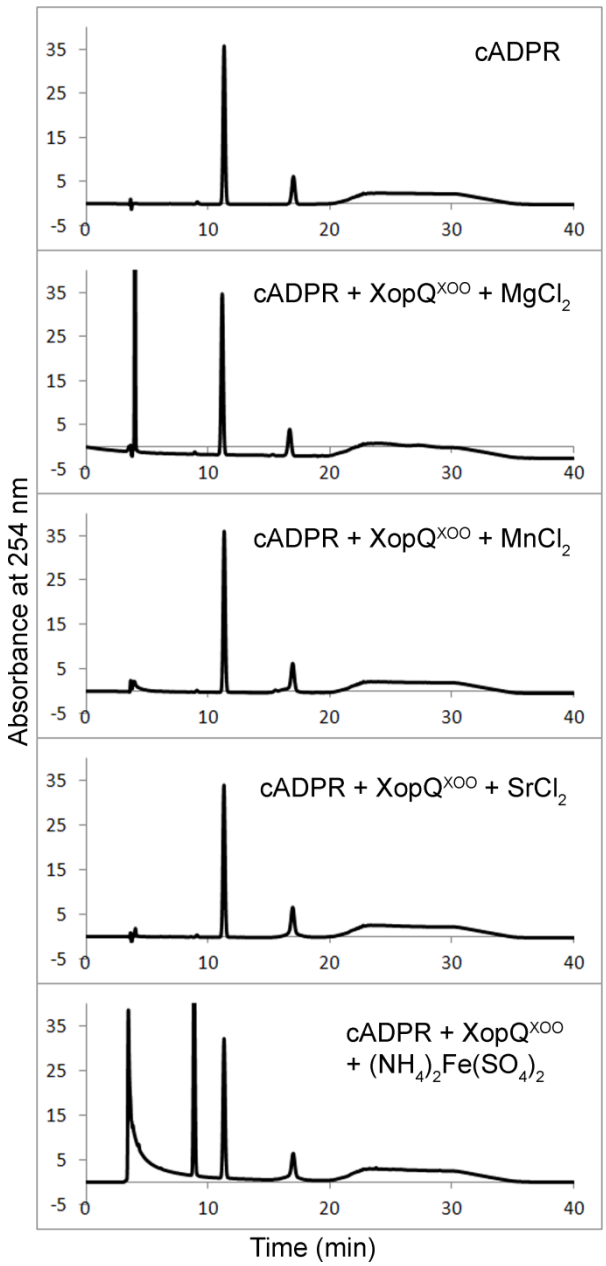
cADPR
cADPR + XopQ^{XOO} + $MgCl_2$
cADPR + XopQ^{XOO} + $MnCl_2$
cADPR + XopQ^{XOO} + $SrCl_2$
cADPR + XopQ^{XOO} + $(NH_4)_2Fe(SO_4)_2$
Absorbance at 254 nm
Time (min)
35
25
15
5
-5
0
10
20
30
40

incubated in a solution containing 50 μM full-length XopQ(FULL)^{XOO}, and the resulting mixture was separated and analyzed by HPLC. If XopQ^{XOO} acts as an ADPR-binding protein, then the elution peak corresponding to ADPR would have been reduced, relative to that obtained in the absence of XopQ^{XOO}. However, the chromatogram obtained from the mixture of XopQ^{XOO} and ADPR was essentially identical to that for ADPR alone (Fig. 17). This suggests that XopQ^{XOO} does not bind ADPR under our experimental conditions. I then attempted to evaluate the binding of XopQ^{XOO} to cADPR using isothermal calorimetric titration, but the experiment was unsuccessful due to the protein solubility of XopQ(FULL)^{XOO}. Since Asp116 in XopQ^{XOO} corresponds to the catalytic residue of NHs, a D116N mutant of XopQ(FULL)^{XOO} was prepared in order to prevent the possible hydrolytic conversion of cADPR to ADPR.

6. Functional implications of XopQ^{XOO}

Recently, several reports have described the various functional aspects of XopQ and HopQ1-1 (Giska et al., 2013; Li et al., 2013; Teper et al., 2014). These studies showed that XopQ and HopQ1-1 interact with host 14-3-3 proteins in a phosphorylation-dependent manner at a conserved serine residue (Ser65 in XopQ^{XOO}), and that these interactions dictate the

Fig. 17. HPLC analyses of ADPR incubated with $XopQ^{XOO}$. HPLC chromatograms are given for ADPR incubated with $XopQ(FULL)^{XOO}$. For the enzyme reaction, 50 μM ADPR was incubated with 50 μM $XopQ(FULL)^{XOO}$ at 25ºC for 40min, and separated and analyzed by HPLC.

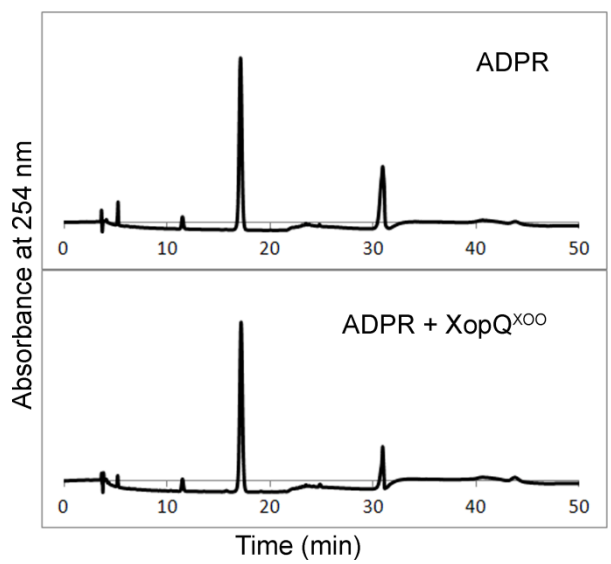
ADPR
ADPR + XopQXOO
Absorbance at 254 nm
Time (min)
0
10
20
30
40
50

localization of effector proteins between the cytoplasm and nucleus. However, the functional role of XopQ remains elusive.

Initially, crystallographic observations of the binding of ADPR in XopQ(D85)^{XOO} provided a plausible explanation for the pathogenic properties of XopQ. cADPR is known as a second messenger for Ca^{2+} signaling in eukaryotic cells (Guse, 2005), and the regulation of cADPR and the Ca^{2+} concentration is one of the key immunological events that occur when a pathogen invades a host plant (Cheval et al., 2013; DeFalco et al., 2010; Durner et al., 1998; Reddy et al., 2011). Therefore, I hypothesized that the cADPR-hydrolytic activity of XopQ^{XOO} could de-sensitize or suppress the host immune system against the intrusion of a pathogen. Under these circumstances, no increase in cytoplasmic Ca^{2+} concentration would occur. However, this study has shown that neither XopQ^{XOO} nor HopQ1-1 exhibited the proposed cADPR-hydrolytic activity. It is still possible that the binding of ADPR is a crystallographic artifact, or XopQ^{XOO} purified from *E. coli* is not obtained in a functionally active form. It might require an as of yet uncharacterized protein modification in the host cell or another process to induce activity. From a structural perspective, the binding of ADPR as a mere crystallographic artifact can be ruled out, because many of the candidates containing a ribose moiety, as well as ribose itself, failed to bind

XopQ^{XOO}. In addition, the conformational changes characterized in this study represent a highly specific response of the enzyme to its ligand. Therefore, further biochemical and/or physiological studies are required to fully obtain a functional assignment of XopQ^{XOO}.

CONCLUSIONS

$XopQ^{XOO}$ is a NH-homologous effector protein from the phyto-pathogen *X. oryzae* pv. *oryzae*. The overall structure of $XopQ(D85)^{XOO}$ is similar with NHs, including a divalent cation-binding site, but its oligomeric state and details in the active site are quite different. In particular, loop-3, one of the major elements in the active site, exhibits a completely different conformation. Therefore, the identity and relative orientations of the active site residues characterized in other NHs no longer match those in $XopQ^{XOO}$, although several residues were proposed as active site residues in $XopQ^{XOO}$.

The crystal structure of $XopQ(D85)^{XOO}$ in a complex with ADPR shows that the 2'- and 3'-hydroxyl groups of ribose$^{\beta}$ are tethered to the Ca^{2+} ion in a manner similar to that of nucleosides bound to NHs. Other residues of $XopQ(D85)^{XOO}$ undergo large conformational changes in order to interact with an adenosyl moiety on the other end of ADPR, effectively sealing off the active site. *In vitro* assays, however, did not show binding of ADPR, nor any hydrolytic activity for cADPR. These data indicate that $XopQ^{XOO}$ is capable of binding a novel chemical bearing a ribosyl moiety and provide the first step toward understanding the functional role of $XopQ^{XOO}$.

REFERENCES

Adams, P.D., Gopal, K., Grosse-Kunstleve, R.H., Hung, L.W., Ioerger, T.R., et al., 2004. Recent developments in the *PHENIX* software for automated crystallographic structure determination. J. Synchrotron. Rad. 11, 53–55.

Adhikari, T.B., Vera Cruz, C.M., Zhang, Q., Nelson, R.J., Skinner, D.Z., et al., 1995. Genetic diversity of *Xanthomonas oryzae* pv. *oryzae* in Asia. Appl. Environ. Microbiol. 61, 966–971.

CCP4, 1994. The CCP4 suite: programs for protein crystallography. Acta Crystallogr. D Biol. Crystallogr. 50, 760–763.

Chen, V.B., Arendall, W.B., Headd, J.J., Keedy, D.A., Immormino, R.M., et al., 2010. MolProbity: all-atom structure validation for macromolecular crystallography. Acta Crystallogr. D Biol. Crystallogr. 66, 12–21.

Cheval, C., Aldon, D., Galaud, J.-P., Ranty, B., 2013. Calcium/calmodulin-mediated regulation of plant immunity. BBA-Mol. Cell Res. 1833, 1766–1771.

Chisholm, S.T., Coaker, G., Day, B., Staskawicz, B.J., 2006. Host-microbe interactions: shaping the evolution of the plant immune response. Cell 124, 803–814.

Christie, P.J., Atmakuri, K., Krishnamoorthy, V., Jakubowski, S., Cascales, E. 2005. Biogenesis, architecture, and function of bacterial type IV secretion systems. Annu. Rev. Microbiol. 59, 451–485.

DeFalco, T.A., Bender. K.W., Snedden, W.A., 2010. Breaking the code: Ca^{2+} sensors in plant signalling. Biochem. J. 425, 27–40.

Degano, M., Almo, S.C., Sacchettini, J.C., Schramm, V.L., 1998. Trypanosomal nucleoside hydrolase. A novel mechanism from the structure with a transition-state inhibitor. Biochemistry 37, 6277–6285.

DeLano, W.L., 2008. The PyMOL molecular graphics system. DeLano Scientific LLC, Palo Alto, CA, USA. <http://www.pymol.org>.

Durner, J., Wendehenne, D., Klessig, D.F., 1998. Defense gene induction in

tobacco by nitric oxide, cyclic GMP, and cyclic ADP-ribose. Proc. Natl. Acad. Sci. USA 95, 10328–10333.

Emsley, P., Cowtan, K., 2004. Coot: model-building tools for molecular graphics. Acta Crystallogr. D Biol. Crystallogr. 60, 2126–2132.

Filloux, A., Hachani, A., and Bleves, S. 2008. The bacterial type VI secretion machine: yet another player for protein transport across membranes. Microbiology 154, 1570–1583.

Furutani, A., Takaoka, M., Sanada, H., Noguchi, Y., Oku, T., et al., 2009. Identification of novel type III secretion effectors in *Xanthomonas oryzae* pv. *oryzae*. Mol. Plant-Microbe Interact. 22, 96–106.

Galán, J.E., Wolf-Watz, H., 2006. Protein delivery into eukaryotic cells by type III secretion machines. Nature 444, 567–573.

Giabbai, B., Degano, M., 2004a. Crystal structure to 1.7 Å of the *Escherichia coli* pyrimidine nucleoside hydrolase YeiK, a novel candidate for cancer gene therapy. Structure 12, 739–749.

Giabbai, B., Degano, M., 2004b. Cloning, purification, crystallization and X-ray analysis of the *Escherichia coli* pyrimidine nucleoside hydrolase YeiK. Acta Crystallogr. D Biol. Crystallogr. 60, 524–527.

Giska, F., Lichocka, M., Piechocki, M., Dadlez, M., Schmelzer, E., et al., 2013. Phosphorylation of HopQ1, a type III effector from *Pseudomonas syringae*, creates a binding site for host 14-3-3 proteins. Plant Physiol. 161, 2049–2061.

Gouet, P., Courcelle, E., Stuart, D.I., Metoz, F., 1999. ESPript: analysis of multiple sequence alignments in PostScript. Bioinformatics 15, 305–308.

Grant, S.R., Fisher, E.J., Chang, J.H., Mole, B.M., Dangl, J.L., 2006. Subterfuge and manipulation: type III effector proteins of phytopathogenic bacteria. Annu. Rev. Microbiol. 60, 425–449.

Gurlebeck, D., Thieme, F., Bonas, U., 2006. Type III effector proteins from the plant pathogen Xanthomonas and their role in the interaction with the host plant. J. Plant Physiol. 163, 233–255.

Guse, A.H., 2005. Second messenger function and the structure-activity relationship of cyclic adenosine diphosphoribose (cADPR). FEBS J. 272, 4590–4597.

Hann, D.R., Domínguez-Ferreras, A., Motyka, V., Dobrev, P.I., Schornack, S., et al., 2014. The Pseudomonas type III effector HopQ1 activates cytokinin signaling and interferes with plant innate immunity. New Phytol. 201, 585–598.

Hendrickson, W.A., Smith, J.L., Sheriff, S., 1985. Direct phase determination based on anomalous scattering. Methods Enzymol. 115, 41–55.

Janjusevic, R., Abramovitch, R.B., Martin, G.B., and Stebbins, C.E. 2006. A bacterial inhibitor of host programmed cell death defenses is an E3 ubiquitin ligase. Science 311, 222–226.

Jiang, W., Jiang, B., Xu, R., Huang, J., Wei, H., et al., 2009. Identification of six type III effector genes with the PIP box in *Xanthomonas campestris* pv.

campestris and five of them contribute individually to full pathogenicity. Mol. Plant-Microbe Interact. 22, 1401–1411.

Kamdar, H., Kamoun, S., Kado, C.I., 1993. Restoration of pathogenicity of avirulent *Xanthomonas oryzae* pv. *oryzae* and *X. campestris* pathovars by reciprocal complementation with the *hrpXo* and *hrpXc* genes and identification of *hrpX* function by sequence analysis. J. Bacteriol. 175, 2017–2025.

Li, W., Yadeta, K.A., Elmore, J.M., Coaker, G., 2013. The *Pseudomonas syringae* effector HopQ1 promotes bacterial virulence and interacts with tomato 14-3-3 proteins in a phosphorylation-dependent manner. Plant Physiol. 161, 2062–2074.

Li, Z., Wan, H., Shi, Y., Ouyang, P., 2004. Personal experience with four kinds of chemical structure drawing software: review on ChemDraw, ChemWindow, ISIS/Draw, and ChemSketch. J. Chem. Inf. Comput. Sci. 44, 1886–1890.

Miller, G.L., 1959. Use of dinitrosalicylic acid reagent for determination of

reducing sugar. Anal. Chem. 31**,** 426–428.

Mudgett, M.B., 2005. New insights to the function of phytopathogenic bacterial type III effectors in plants. Annu. Rev. Plant Biol. 56, 509–531.

Niño-Liu, D.O., Ronald, P.C., Bogdanove, A.J., 2006. *Xanthomonas oryzae* pathovars: model pathogens of a model crop. Mol. Plant Pathol. 7, 303–324.

Nurnberger, T., Brunner, F., Kemmerling, B., Piater, L. 2004. Innate immunity in plants and animals: striking similarities and obvious differences. Immunol. Rev. 198, 249–266.

Otwinowski, Z., Minor, W., 1997. Processing of X-ray diffraction data collected in oscillation mode. Methods Enzymol. 276, 307–326.

Pawlikowska, L., Cottrell, S.E., Harms, M.B., Li, Y., Rosenberg, P.A., 1996. Extracellular synthesis of cADP-ribose from nicotinamide-adenine dinucleotide by rat cortical astrocytes in culture. J. Neurosci. 16, 5372–5381.

Pettersen, E.F., Goddard, T.D., Huang, C.C., Couch, G.S., Greenblatt, D.M.,

et al., 2004. UCSF Chimera--a visualization system for exploratory research and analysis. J. Comput. Chem. 25, 1605-1612.

Pieterse, C.M.J., Leon-Reyes, A., Van der Ent, S., C M Van Wees, S., 2009. Networking by small-molecule hormones in plant immunity. Nature Chem. Biol. 5, 308–316.

Reddy, A.S.N., Ali, G.S., Celesnik, H., Day, I.S., 2011. Coping with stresses: roles of calcium- and calcium/calmodulin-regulated gene expression. Plant Cell 23, 2010–2032.

Roden, J.A., Belt, B., Ross, J.B., Tachibana, T., Vargas, J., et al., 2004. A genetic screen to isolate type III effectors translocated into pepper cells during *Xanthomonas* infection. Proc. Natl. Acad. Sci. U.S.A. 101, 16624–16629.

Shi, W., Schramm, V.L., Almo, S.C., 1999. Nucleoside hydrolase from *Leishmania major*. J. Biol. Chem. 274, 21114–21120.

Sinha, D., Gupta, M.K., Patel, H.K., Ranjan, A., Sonti, R.V., 2013. Cell wall

degrading enzyme induced rice innate immune responses are suppressed by the type 3 secretion system effectors XopN, XopQ, XopX and XopZ of *Xanthomonas oryzae* pv. *oryzae*. PLoS One 8, e75867.

Stebbins, C.E., and Gala´ n, J.E. 2001. Structural mimicry in bacterial virulence. Nature 412, 701–705.

Teper, D., Salomon, D., Sunitha, S., Kim, J.-G., Mudgett, M.B., et al., 2014. *Xanthomonas euvesicatoria* type III effector XopQ interacts with tomato and pepper 14–3–3 isoforms to suppress effector-triggered immunity. Plant J. 77, 297–309.

Terwilliger, T.C., 2000. Maximum-likelihood density modification. Acta Crystallogr. D Biol. Crystallogr. 56, 965–972.

Terwilliger, T.C., Berendzen, J., 1999. Automated MAD and MIR structure solution. Acta Crystallogr. D Biol. Crystallogr. 55, 849–861.

Vandemeulebroucke, A., Minici, C., Bruno, I., Muzzolini, L., Tornaghi, P., et al., 2010. Structure and mechanism of the 6-oxopurine nucleosidase from

Trypanosoma brucei brucei. Biochemistry 49, 8999–9010.

Versées, W., Decanniere, K., Holsbeke, E.V., Devroede, N., Steyaert, J., 2002. Enzyme-substrate interactions in the purine-specific nucleoside hydrolase from *Trypanosoma vivax*. J. Biol. Chem. 277, 15938–15946.

Versées, W., Decanniere, K., Pellé, R., Depoorter, J., Brosens, E., et al., 2001. Structure and function of a novel purine specific nucleoside hydrolase from *Trypanosoma vivax*. J. Mol. Biol. 307, 1363–1379.

Wei, C., Kvitko, B.H., Shimizu, R., Crabill, E., Alfano, J.R., et al., 2007. A *Pseudomonas syringae* pv. *tomato* DC3000 mutant lacking the type III effector HopQ1-1 is able to cause disease in the model plant *Nicotiana benthamiana*. Plant J. 51, 32–46.

Zhang, J., Zhou, J-M., 2010. Plant immunity triggered by microbial molecular signatures. Mol. Plant 3, 783–793.

국문초록

많은 그램음성균들은 secretion system을 이용하여 그들의 virulence factor를 숙주세포 안으로 분비한다. Effector라고 불리는 이런 분비 물질들은 숙주세포 안에서 일어나는 다양한 일들을 저해함으로써 세포의 병원성과 깊게 관련되어 있다. 벼 흰잎마름병을 일으키는 *Xanthomonas oryzae* pv. *oryzae*는 type III secretion system을 이용하여 effector를 주입하지만 이런 effector 단백질들의 기능은 아직까지 잘 알려져 있지 않다. 서열 유사성의 분석을 통하여 *X. oryzae* pv. *oryzae*의 type III effector 단백질인 $XopQ^{XOO}$와 다른 식물 병원균의 유사단백질들은 뉴클리오시드 가수분해효소 (NH)일 것으로 예상되었다. 실제로 이가 양이온 결합 부위를 포함한 $XopQ^{XOO}$의 전체적인 구조는 NH의 구조와 유사하지만 oligomeric state와 활성 부위의 topology는 사뭇 다르다. NH의 공통된 특징인 활성 부위의 loop에 인접한 antiparallel β-strand는 $XopQ^{XOO}$의 경우 짧은 loop으로 대체됨으로써, NH의 활성 부위의 loop과는 확실히 구별되는 conformation을 초래한다. 따라서 NH의 활성 부위의 loop에 위치한

잔기들은 $XopQ^{XOO}$의 예상되는 활성 부위에 존재하지 않는다. 이러한 구조적 특징들과 일치하게 기능 연구의 결과는 $XopQ^{XOO}$가 NH의 활성을 나타내지 않음을 보여준다.

리보스 결합 부위의 Ca^{2+} coordination shell이 NH와 완벽하게 일치한다는 점과 눈에 띄는 널찍한 활성 부위를 가지고 있다는 점은 ribose를 포함하는 새로운 물질이 $XopQ^{XOO}$의 기질일 가능성을 시사한다. 이에 부합하게 진핵세포질내의 Ca^{2+} 농도의 조절에 관련된 adenosine diphosphate ribose (ADPR)과 $XopQ^{XOO}$의 결합체 구조를 결정할 수 있었다. $XopQ^{XOO}$의 활성 부위에 위치한 ADPR의 ribosyl end는 Ca^{2+} coordination shell과 결합한다. 그리고 ADPR의 결합은 ligand-induced conformational change로 인하여 인접한 소수성 잔기들에 의하여 더욱 안정화된다. 기능 연구와 함께 이러한 데이터는 ribose를 포함하는 새로운 물질과 결합할 수 있는 $XopQ^{XOO}$의 가능성을 보여주며, 이것은 $XopQ^{XOO}$의 기능을 이해하기 위한 첫 단계일 것이다.

주요어: effector 단백질; 병원성; type III secretion system; *Xanthomonas* outer protein Q; 뉴클리오시드 가수분해효소; adenosine diphosphate ribose

학 번: 2007-21398

CURRICULUM VITAE

Name : Sangheon Yu

Sex : Male

Date of Birth : August 19, 1980

Place of Birth : Daejeon, Korea

Present Address : Graduate school of Agricultural Biotechnology
Seoul National University
Seoul 151-921, Korea
Phone: 82-2-880-4633
Fax: 82-2-873-3112
E-mail: shyu@snu.ac.kr

Education : Chungnam National University
Daejeon, Korea
B.S. in Department of Biochemistry (2006)

Seoul National University
Seoul, Korea
Ph.D. in Agricultural Biotechnology (2014)